Friedrich-Alexander-Universität
Faculty of Sciences

Bachelor’s thesis

06-03-2026

Lea Schneidhuber

Supervisor: Prof. Dr. Anna Nelles

Solar Fares in LOFAR Cosmic Ray Mode

Abstract

The LOw Frequency ARray (LOFAR) is primarily used for astronomical observations and additionally detects Cosmic Rays (CRs) by measuring the radio emission from extensive air showers in the 10^{16} eV to $10^{18.5}$ eV energy range. This thesis focuses on determining if solar flares were detected while being in LOFAR Cosmic Ray (CR) mode in the years $2012 - 2024$ and analyzing possible solar flare detections. The data of the GOES satellites is used for the determination of solar flare candidates. For the analysis of the LOFAR data, we made interferometric sky maps and dynamic spectra which we compared to the data of other observatories. The LOFAR data allows a nanosecond time scale investigation of the signals. We found multiple coincidences of LOFAR CR events with solar flares, with one event showing clear signatures of a solar flare - the second largest flare in solar cycle 24 on 09/10/2017 - in its dynamic spectrum. Additionally, the time domain data of this LOFAR event was examined and a "pulsed" structure was found. For a probability analysis, the expected number of LOFAR-event-matches with daytime solar flares is calculated and compared to the actual number of matches. It is found that the expected numbers are lower than the actual numbers which has various reasons that are discussed in the scope of the thesis.

Contents

1 Introduction

"While observing a group of solar spots on the 1st September, I was suddenly surprised at the appearance of a very brilliant star of light, much brighter than the sun's surface, most dazzling to the protected eye, illuminating the upper edges of the adjacent spots and streaks, not unlike in effect the edging of the clouds at sunset; the xrays extend in all directions." - by R. Hodgson in 1859 about a curious appearance he has seen in the Sun [1].

What was originally considered as white-light brightenings, is now known as solar flares that extend across the entire electromagnetic spectrum. Solar flares appear in various forms and differ a lot in their energy, form and length. Even though the solar flare's essential nature - the explosive release of energy stored in current-carrying magnetic fields in the outer solar atmosphere - is generally accepted, the processes and the events through which this stored energy is released, are far from fully understood. Through these still poorly understood physical processes, the energy is, among other things, converted into three energetically important products: Hot plasma, erupting material and accelerated particles (e^-, ions). Since the radiation emitted by solar flares covers the entire electromagnetic spectrum, our level of knowledge came through detecting and analyzing the emission across this wide wavelength band which provides a lot of information about the different physical processes that produce this kind of emission. On the other hand, the wide frequency band is very challenging since each few decades of wavelength and energy require different detection technologies and an understanding of the different radiation mechanisms [2].

The generated shocks and high-energy particles can propagate through the heliosphere, may influence planetary ionospheres (cf. [3]) and have a strong influence on space weather and therefore can affect global communication technology on which we increasingly rely (cf. [4]). These powerful eruptions can even influence the habitability of exoplanets (cf. [5]). Since solar flares have such a high influence on a lot of different things, it is of crucial importance to study the physics behind them to understand better our surroundings and potentially other star systems.

With its 52 stations distributed all over Europe, the LOw Frequency ARray (LOFAR) is the world's largest radio telescope (cf. [6]). It is primarily used for astronomical observations and additionally detects Cosmic Rays (CRs) by measuring the radio emission from the extensive air showers that they trigger in the atmosphere. With its low-frequency coverage combined with a high resolution, LOFAR offers a powerful tool for probing unexplored solar coronal structures [4].

The goal of this thesis is to determine if we detected solar flares in the LOFAR CR mode in the past years ($2012 - 2024$). The first step is to find the solar flares of these years by using the data of other instruments. With that, we want to analyze the LOFAR data and search for possible coincidences with strong solar activities and flares. Additionally, we want to determine how many LOFAR-event-matches with solar flares we expect for this time period and compare the expectation to the actual data. If we detected a solar flare while being in CR mode, the aim is to characterize and analyze the signal further and compare it to the data of other observatories.

2 Solar Flares

This chapter will introduce solar flares, their emission mechanism, their characterization and frequency. In addition, some solar observatories are briefly introduced.

2.1 What are Solar Flares?

Solar flares are the most powerful magnetic events in the solar system. They emit radiation across the entire electromagnetic spectrum, from radio to gamma-rays [7].
It is generally accepted that solar flares and their often-associated Coronal Mass Ejections (CMEs) are connected to the energy that is stored in the magnetic field of the solar corona. Within hours or days, a very high energy builds up within a so-called active region, which covers a small fraction of the solar disk. It is instantaneously and impulsively released through the underlying process of CMEs and solar flares, the magnetic reconnection. The magnetic reconnection refers to oppositely directed magnetic field lines which come together and merge. In a large solar flare, the reconnection enables the magnetic field to relax to a lower energy configuration in the process by transferring more than 10^{32} erg of energy.
Solar flares and their CME are usually called a "solar eruptive event" (SEE). The current understanding of a SEE is shown in Figure 1. The released energy of the magnetic reconnection goes into accelerating charged particles (e^-, p and heavier ions), the heating of the coronal plasma and leads to a drift of the flux rope away from the Sun which then becomes a CME. Due to electromagnetic forces, the particles accelerated in the downward direction are torn on a spiral along the magnetic field lines until they reach the "loop footprints" in the higher - density region of the lower corona and upper chromosphere [2].

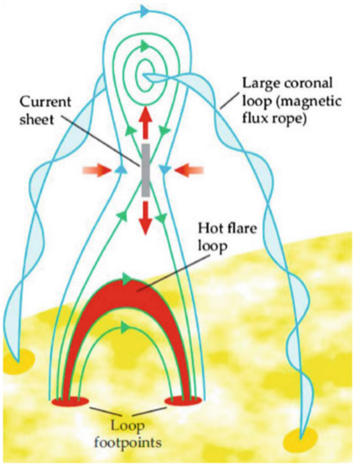

Figure 1: Principle of a SEE. Magnetic field lines (blue) come out of the solar photosphere (yellow) and pass into the corona. A few of them are drawn into a current sheet where magnetic reconnection takes place and therefore energy is released. New reconnected field lines (green) that move downwards produce hot flare loops (red). The ones moving upwards add to the flux rope (light blue) that connects back to the solar surface. Figure taken from [2].

2.2 Characterization of Solar Flares

Solar flares differ a lot in their energy, form and length. Therefore, a classification is needed to distinguish them. The primary way of classifying a flare is via its soft X-ray flux at $1 - 8\,\text{Å}$ as measured by for example Geostationary Operational Environmental Satellites (GOES). Flares are therefore classified into X, M, C, B and A flares, with X flares having the largest and A flares having the smallest peak strengths. X flares correspond to a peak flux of more than $10^{-4}\,\frac{\mathrm{W}}{\mathrm{m}^2}$, the other classifications decrease in decades [7]. X, M and C flares refer to "x-treme", "medium" and "common" flares. Each classification is subdivided using numbers after the classification such as C4.2 or X2.2 which corresponds to a flux of the number multiplied by the threshold flux of the respective classification. X2.2 would then correspond to a flux of $2.2 \cdot 10^{-4}\,\frac{\mathrm{W}}{\mathrm{m}^2}$ [8].

Solar radio bursts are divided into five general classes I − V based on their temporal and spectral characteristics. This terminology developed historically [9].

Type I bursts are short (second - long) quasi-monochramatic spikes with huge variation in intensity over the $80 - 200\,\mathrm{MHz}$ frequency range. They are related to active hot spots on the solar surface. They usually cluster as "noise storms" which can last for a few hours up to a few days and sometimes show a continous underlying broadband emission. Even though single signals show no noteworthy drift in frequency, the temporally spiking emissions tend to evolve towards lower frequencies in a storm.

Type II bursts are usually associated with electron acceleration in the shock fronts at the leading edge of CMEs. They can last a few minutes during which the narrow-band emission of the fundamental (harmonic) mode slowly drifts from $\approx 150\,\mathrm{MHz}$ to lower frequencies. Typical drift rates for these flares are $\approx 0.05\,\frac{\mathrm{MHz}}{\mathrm{s}}$.

Type III bursts are believed to be emitted by relativistic electron beams $(0.1 - 0.3\,\mathrm{c})$ traveling along open magnetic field lines during CME events. This type of bursts only occurs in isolation or in clusters. They last for a few seconds and show drift rates up to $1\,\frac{\mathrm{GHz}}{\mathrm{s}}$. Rarely, they do not continue to drift to lower frequencies towards the end of the flaring period, but show an inverted "J" or "U" structure in their dynamic spectra. These "U" and "J" subtypes refer to the case, when electrons do not escape along the open magnetic field lines but instead propagate downwards along a closed loop within the solar corona.

Type IV and V bursts are rare and occur never in isolation. Type IV bursts form a smooth continuum of broad-band bursts beginning $10 - 20\,\mathrm{min}$ after the flare maximum of some major flare events, with hour-scale duration. Type V bursts are short-lived continous noise at the lower frequency tail below $200\,\mathrm{MHz}$ and follow in rare cases a type III burst ([10], [11]).

For our work, type X solar flares are most relevant due to the fact that these flares show long-lasting radiation storms and have the highest peak strengths (cf. [12]).

Type I radio bursts are not relevant for this thesis, since their frequency range does not match with the frequency range of the Low-Band Antenna (LBA) (cf. subsection 3.1) [4]. Type II and type III bursts occur at low frequencies and therefore are important for our work (cf. [13] and [10]).

2.3 Solar cycle and Frequency of Solar Flares

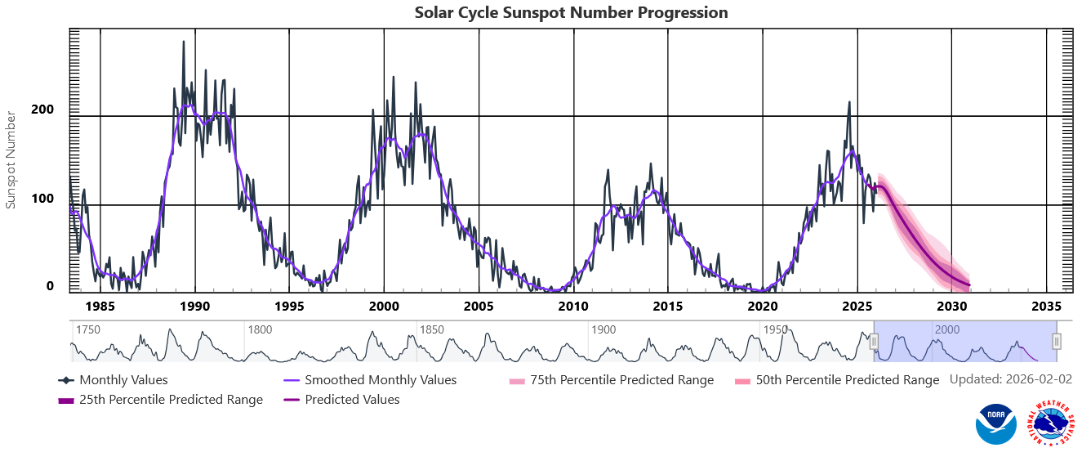

Figure 2: Variability of the sun spots during the solar cycle for the years 1985 – now. The purple line presents a prediction of the solar cycle for the next years. Figure taken from [14].

The solar activity is variable as a function of time. A full solar cycle has a duration of 22 yrs. With the solar activity, the number of sunspots varies in the same periodicity (cf. Figure 2). As the cycle progresses, the Sun's activity builds up to a maximum and settles back to a minimum when a new cycle begins. It is observed that the polarity of the magnetic field of the sun switches every 11 yrs. Furthermore, the frequency of the solar flares also coincides with the solar cycle: When the solar cycle is at its minimum, active regions are small and rare and only a few solar flares are observed. Hence, the number of solar flares increases as the solar cycle reaches its maximum, because fast CMEs occur also more often near the peak of the solar cycle [15].
In this thesis, data of the years 2012 – 2024 is discussed. As shown in Figure 2, the solar cycle reached its maximum in the year 2014, decreased and reached its minimum in 2020. Then the next solar maximum began in the year 2024.

2.4 Solar Observatories

In the following chapters, a few instruments that are (continuously) monitoring the sun, are described.

2.4.1 Callisto

Callisto stands for Compound Astronomical Low frequency Low cost Instrument for Spectroscopy and Transportable Observatory (cf. [16]). The goal of Callisto is understanding transient phenomena in the solar corona. The ground-based Callisto spectrometer is a programmable heterodyne receiver that was designed in 2006, which operates between 45 MHz and 870 MHz. All Callisto spectrometer together form the e-Callisto network, which is distributed all over the world and makes a continuous observation of the solar radio spectrum for 24 h per day all through the year possible.

It consists of over 220 observatories, of which on average around 80 provide daily public open-source radio spectrograms. In Figure 3 all Callisto instruments are shown [17].

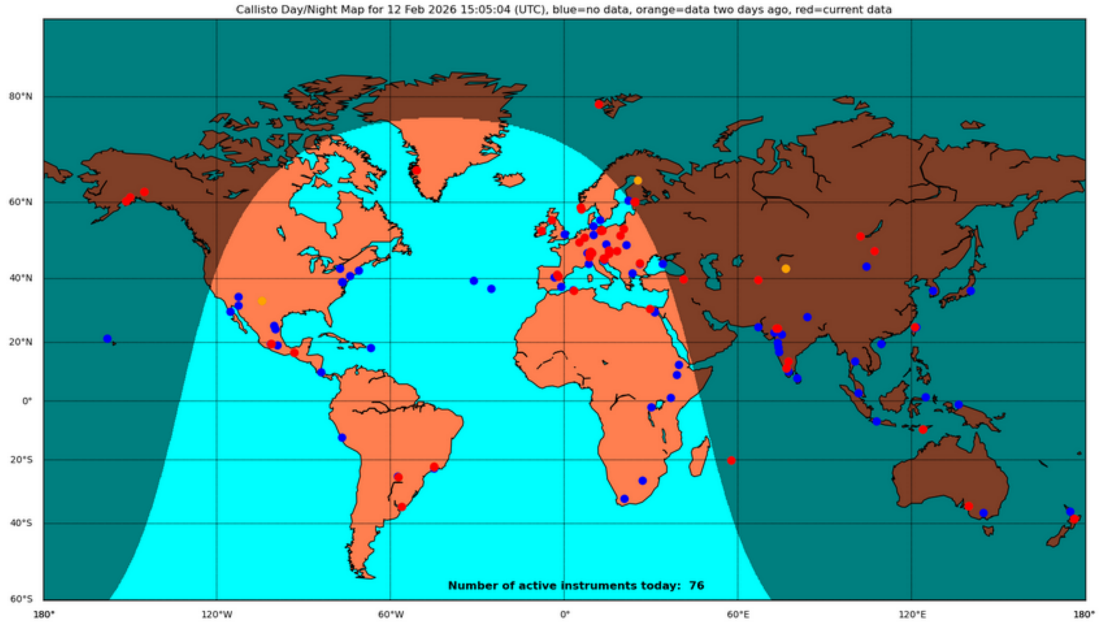

Figure 3: World map with all Callisto instruments (one dot can represent up to 5 instruments). Day/Night map of 02/12/2026 15:05:04. Figure taken from [17].

2.4.2 GOES

Geostationary Operational Environmental Satellites (GOES) have been observing terrestrial weather, space weather, including solar flares, SEEs and the space environment (fields and particles) since 1975. For the space weather observations, there are two identical operational GOES satellites of the National Oceanic and Atmospheric Administration (NOAA) in geostationary orbit, one at 75.2 ° longitude west and one at 132.2 ° longitude west and at least one on-orbit back-up satellite [18].
The GOES-R series includes four satellites: GOES-R (cf. [19]), GOES-S (cf. [20]), GOES-T (cf. [21]), and GOES-U (cf. [22]), which were launched on 9 November 2016, 1 March 2018, 1 March 2022, and 25 June 2024, respectively and named GOES-16, 17, 18, and 19, respectively. Out of these, GOES-16 and GOES-18 are the primary operational satellites.
The Geostationary Orbiting Environmental Satellites X-Ray Sensor (GOES-XRS) measures the full-disk solar X-ray irradiance in two wavelength intervals: XRS-A (”short channel”, $\Delta\lambda = 0.05 - 0.4\,\text{nm}$) and XRS-B (”long channel”, $\Delta\lambda = 0.1 - 0.8\,\text{nm}$) [18].

2.4.3 RNO-G

Radio Neutrino Observatory Greenland (RNO-G) (cf. [23]) is a radio observatory that is currently under construction near Summit station in Greenland and will consist of an array of hundreds of radio antennas embedded in the glacial ice. The primary goal of RNO-G is measuring astrophysical neutrinos with energies exceeding $10^{15}\,\text{eV}$.
It recently analyzed signals from the sun and solar flares (cf. [11]).

The different antenna types in the RNO-G stations cover a bandwidth of 80 − 700 MHz which overlaps with solar radio emission and have a sampling rate of 3.2 GHz. These solar signals can be a possible contamination but can also be used as a calibration tool. There are 35 stations planned on a square grid with interstitial spacing of 1.25 km (cf. Figure 4). Each station has its own independent neutrino detector and consists of 24 antennas. Moreover, each station combines long-periodic dipole antennas (LPDA) close to the surface with fat-dipoles (Vpol) and quad-slot antennas (Hpol) on instrumented rings down to 100 m below the surface [11].

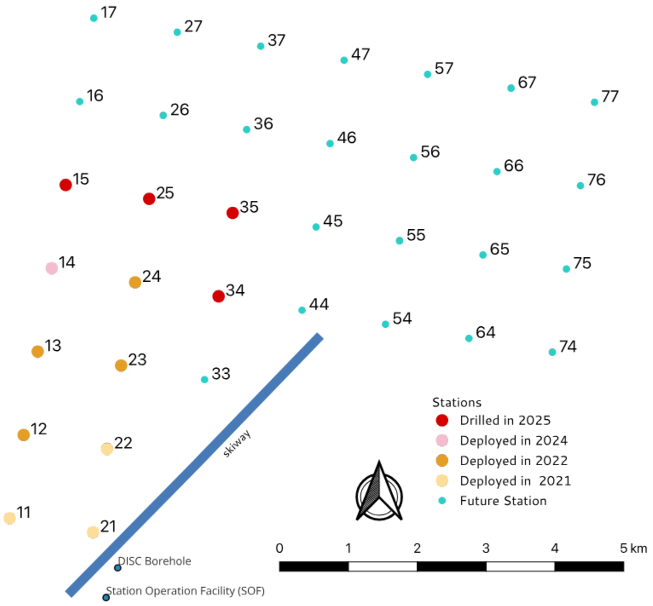

Figure 4: Planned station layout of RNO-G. The "Big house " stands for the main building of Summit station. The light blue line represents the landing stripe for airplanes. Figure taken from [24].

3 LOFAR

In this chapter, the LOw Frequency ARray and its CR observation mode are described, as well as solar flare observations with LOFAR.

3.1 What is LOFAR?

Figure 5: Picture of the Superterp, the heart of the LOFAR core. There are 6 core stations on a large circular plateau, as well as 3 additional stations visible. Figure taken from [4].

The LOw Frequency ARray (LOFAR) (cf. [4]) is the world's largest radio telescope, as it consists of 52 stations distributed all over Europe and each station being a large antenna field spanning over several hundred meters. 24 out of these stations form a dense core in the Netherlands. The Superterp is a collection of 6 of the 24 core stations on a large circular plateau (cf. Figure 5)[6]. There are in total 38 stations in the Netherlands, 6 stations in Germany, 3 stations in Poland and one station each in France, Ireland, Lativa, Sweden and the United Kingdom. There are stations in Italy and Bulgaria soon to be built (cf. Figure 7). The huge range of distances between the stations yield unique capabilities for detailed images of the sky [25].
Primarily used for astronomical observations, it additionally detects Cosmic Rays (CRs) by measuring the radio emission from extensive air showers in the 10^{16} eV to $10^{18.5}$ eV range which is precisely the expected transition region from galactic to extragalactic CRs. The measured radio emission stems from the dominant geomagnetic effect and the sub-dominant Askaryan-effect (cf. [6]).
LOfar Radboud air shower Array (LORA) is installed in the core of LOFAR in the Netherlands. It contains 20 detector units that are located on a circular area with a diameter of 320 m. The Superterp area is thus subdivided into five units, each containing

four detectors. The detectors are placed on circles with a radius of about 40 m around a central electronics unit with a distance of $50 - 100$ m between the detectors. One detector unit consists of two pairs of scintillators and two Photo Multiplier Tubes (PMTs) [26].

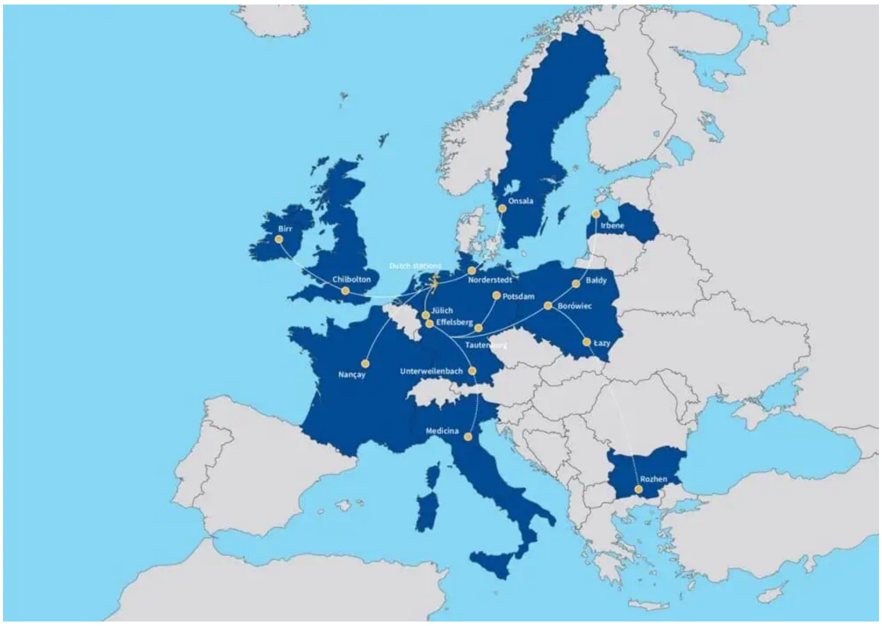

Figure 6: Map of all 52 LOFAR stations including the one in Italy and Bulgaria that are soon to be build. Figure taken from [25].

3.1.1 Different LOFAR Stations

All the LOFAR stations contain antennas, digital electronics and local computing resources. LOFAR stations are classified as either core, remote or international, corresponding to their distance from the center of the array and different antenna field configurations (cf. Figure 6).

Core stations contain 96 Low-Band Antenna (LBA) and two times 24 High-Band Antenna (HBA). These core HBA sub-stations can be used either as a single station or separately as independent LOFAR stations. Remote stations have two times 48 LBAs and 48 HBAs. Each core and remote station has 48 digital Receiver Units (RCUs), which represent the beginning of the digital signal path and feature three distinct inputs per board. For core and remote stations, two of these inputs are assigned to the 96 LBA dipoles and the remaining input is used for the 48 HBA tiles. The restriction of LOFAR1.0 is that only one of these three inputs can be active at one time. That means that 48 HBA tiles can be used at once, but only half of the 96 LBA dipole signals can be processed at a given time. That is why LBA dipoles are grouped into "LBA inner" (inner circle) and "LBA outer" (outer annulus) configurations. These result in different FoVs and can be selected by the observer during the observation specification process.

The international LOFAR stations consist of 96 LBAs, HBAs and RCUs each. The additional RCUs provide a total of 192 digital signal paths such that the full set of HBA tiles or LBA dipoles can be used at any given observation [4].

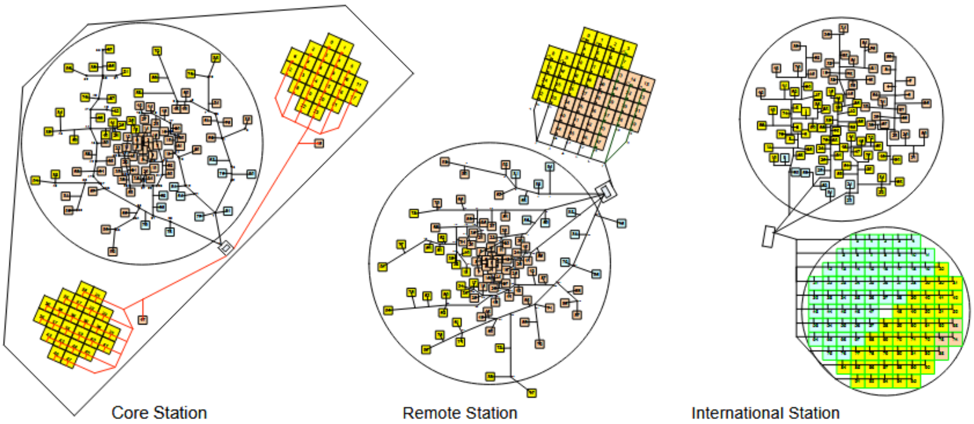

Figure 7: Three different station layouts: Core station, Remote station and International station. The large circles indicate LBA antennas, the array of small squares mark the HBA tiles. The size of the stations can not be compared as they are shown on different spatial scales. Figure taken from [4].

3.1.2 Antennas of LOFAR

As already mentioned in the chapter before, there are two types of antennas for LOFAR: The Low-Band Antenna (LBA) and the High-Band Antenna (HBA). The LBAs are utilized at the lowest frequencies. The frequency range is operationally set to $30 - 80$ MHz by default. The response below 30 MHz is suppressed by an analog filter.

Each LBA element is sensitive to two orthogonal linear polarizations which are detected by using two copper wires that are connected at the top of the antenna to a molded head containing a Low-Noise Amplifier (LNA). Each polarization has its own output, hence two coaxial cables per LBA element run through the vertical PVC pipe on which the molded head rests. The peak of the response curve is at 58 MHz.

The HBA frequency range is operationally limited to $110 - 240$ MHz. The HBA design clusters 16 antenna elements together into tiles which contain initial analog amplification and a first stage of analog beam-forming. The single beam is then formed by combining the signals from these 16 antennas in phase for a given direction on the sky. In contrast to the effectively passive LBAs, since they require power but no active control or synchronization, the HBAs include tile-level beam-forming and are subject to the monitoring and control system MAC. The resulting signals are transported over coaxial cables to the receiver unit, just like for the LBAs [4].

3.1.3 LOFAR2.0

LOFAR is currently upgraded to LOFAR2.0 (cf. [27]). Due to the fact that the HBA data was not usable for the detection of CRs, the total CR mode uptime was below the 100 % duty cycle radio detection promises. The most important proposed change for CR detection is the option to observe with unbeamformed HBA antennas and to have multiple antenna sets available for each observation. This would allow simultaneous measurement of LBAs and HBAs after the upgrade. As a result, it would provide access to the $120 - 240$ MHz band during each measurement. This would not only increase the bandwidth and the uptime, but also provide a known observation time which makes it

possible to determine the observed CR flux. There will also be improvements made to the network which will lead to more event readout and more frequent triggering.
In total, this upgrade will increase the total number of usable events, will provide more information to the events (bandwidth, number of detectors) and will increase the energy range in which it is possible to measure. As a result, that would lead to a high-quality event catalogue to use for different analyses.

3.2 LOFAR Cosmic Ray Mode

LOFAR is capable of measuring in a frequency range of $10-240\,\mathrm{MHz}$ which corresponds to wavelengths of $30-1.2\,\mathrm{m}$ and has a large Field of View (FoV) due to effectively all-sky coverage of the component dipoles [4].
The measurement of CRs happens in the background of regular, scheduled observations of LOFAR. Radio data is continuously buffered by the antennas. If a CR is detected which means it is triggered by the in-situ particle detector LORA, the buffers are frozen and the data is read out. As long as the data outread does not happen that often (about once per hour), there will be no interruption of the ongoing measurements [27].
LORAs main purpose is to trigger a read-out of LOFAR antennas to register extensive air showers. The signals from the antennas are stored in a ring buffer (Transient Buffer Board (TBB)). A triggered read-out will then send the raw data to a central processing facility. For data taking, there is a coincidence trigger condition for three out of four detectors set for each sub-array [26]. For every detected Cosmic Ray event, 2.1 ms of radio data are stored [28].
The TBB provides access to a snapshot of the running data streams of the LBA or HBA antennas. Each TBB can store 1 GB of data for up to 8 dual-polarized antennas either before or after conversion to sub-bands. At station level, each TBB constantly runs a monitoring algorithm on the incoming data-stream, which generates a continuous stream of event data that is received [4].

3.3 Solar flare observations with LOFAR

LOFAR is well suited for studying active processes in the sun's corona with its spectroscopic and imaging capabilities. For that purpose, a key science project named "Solar Physics and Space Weather with LOFAR" was founded [25].
LOFAR can achieve an angular resolution of a few 10 arcseconds. The limiting factor is the scattering in the solar corona. By using the Superterp station, direct snapshot imaging of radio emission of CMEs can be enabled. Moreover, it is possible to use a grid of many tied-array beams to form maps of radio emission covering a broad area around the sun. These maps may have a lower spatial resolution than the ones from direct imaging, but they have the advantage of having a high time and frequency resolution using the beam-formed mode. The types of radio bursts formed in the CME can be easily determined via dynamic spectra.
There are also various analysis techniques that probe the solar wind and different solar wind structures via observing the interplanetary scintillation. As a result, LOFAR enables an observation of both, the solar corona and the interplanetary space with unprecedented spatial and temporal resolution. The observation with LOFAR is incomparable to other instruments (e.g. optical) regarding plasma processes in the corona of the Sun and the solar wind. Through these observations, the concept of

CMEs can be understood better, looking at its initiation, launch, development and propagation through interplanetary space. This is very important for understanding many aspects of Space Weather [4].

4 Probability of Observation

In this chapter, the number of expected LOFAR events during solar flares for the years $2012 - 2024$ is calculated and the results are further investigated.

4.1 Calculation of the Probability

The goal is to calculate the number of expected LOFAR events during daytime solar flares for the years $2012 - 2024$. To find potential timeframes with strong solar activity in which we expect radio emission, we use data from GOES of the past years and search for all the flares that are above a threshold flux of $10^{-4}\,\frac{\mathrm{W}}{\mathrm{m}^2}$. The times when the flares begin or stop are defined as the times when the measurement points meet an arbitrary threshold of $10^{-5}\,\frac{\mathrm{W}}{\mathrm{m}^2}$. All the GOES data flare candidates that were found are shown in subsection A.1

We make the assumption that the number of solar flares in one year and the number of LOFAR events of that year are stochastically independent. Moreover, we assume that the LOFAR events are uniformly distributed.

Furthermore, we define daytime as the time where the sun at the LOFAR location is more than $5\,^\circ$ above the horizon. Then, the total daytime T_{total} of one respective year can be calculated.

As already mentioned in subsection 3.2, the time of one LOFAR event is $t_{\text{event}} = 2.1\,\mathrm{ms}$. With that, the number of $2.1\,\mathrm{ms}$ intervals in the daytime of one year can be calculated to:

$$N_{\text{intervall}} = \frac{T_{\text{total}}}{t_{\text{event}}}. \tag{1}$$

Then, the probability for one event to happen at daytime in one year is

$$P_{\text{event}} = \frac{N_{\text{event}}}{N_{\text{intervall}}} \tag{2}$$

with N_{event} being the number of LOFAR events during daytime in one specific year. Now, the expected number of event matches can be calculated with

$$N_{\text{exp}} = P_{\text{event}} \cdot \frac{T_{\text{flare}}}{t_{\text{event}}} \tag{3}$$

with T_{flare} being the total time of all solar flares of one specific year at daytime. We use T_{flare} instead of $T_{\text{flare}} + t_{\text{event}}$ as we assume that $t_{\text{event}} << T_{\text{flare}}$. This is an appropriate approximation, as the solar flares are minutes to hours long, while the LOFAR event duration is only milliseconds.

In the following, an example calculation of the year 2012 is presented in detail.

The total daytime of the year 2012 was $T_{\text{total}} = 3.15 \cdot 10^{10}\,\mathrm{ms}$. Then, the number of $2.1\,\mathrm{ms}$ intervals in the daytime of that year can be calculated as follows:

$$N_{\text{interval}} = \frac{3.15 \cdot 10^{10}\,\mathrm{ms}}{2.1\,\mathrm{ms}} = 1.50 \cdot 10^{10}. \tag{4}$$

The number of LOFAR events in 2012 is $N_{\text{event}} = 1114$. Then the probability for one event to happen at daytime in 2012 can be calculated to

$$P_{\text{event}} = \frac{1114}{1.50 \cdot 10^{10}} = 7.43 \cdot 10^{-8} \tag{5}$$

The total time of daytime solar flares 2012 is $T_{\text{flare}} = 2.55 \cdot 10^7$ ms based on the GOES data. The number of expected matches for 2012 results in

$$N_{\text{exp, 2012}} = 7.43 \cdot 10^{-8} \cdot \frac{2.55 \cdot 10^7\,\text{ms}}{2.1\,\text{ms}} = 0.90. \tag{6}$$

The calculated expected matches of the years 2012 − 2024 are listed in the following table:

Year	N_{exp}	N_{actual}
2012	0.90 ± 0.95	8
2013	0.51 ± 0.72	2
2014	1.09 ± 1.04	4
2015	0.39 ± 0.62	0
2016	0.07 ± 0.27	0
2017	1.36 ± 1.17	10
2018	0 ± 0	0
2019	0 ± 0	0
2020	0 ± 0	0
2021	0.01 ± 0.08	0
2022	0.02 ± 0.16	0
2023	0 ± 0.06	0
2024	0.38 ± 0.62	0

Table 1: Calculated expected number of LOFAR event matches for the years 2012 − 2024. N_{actual} is the actual number of matches.

The uncertainty of the expected numbers in Table 1 can be calculated with

$$\sigma_N = \sqrt{N_{\text{exp}}}. \tag{7}$$

We use Poisson statistics since we have low numbers of events which excludes the usage of a Gaussian distribution.
Furthermore the number of expected LOFAR event matches for the time period of 2012 − 2024 can be calculated by summing up the expected numbers of Table 1 to

$$N_{\text{exp, tot}} = 4.74 \pm 2.18.$$

Therefore, the uncertainty was calculated by

$$\sigma_{N,\text{ tot}} = \sqrt{\sum_{\text{i=2012}}^{2024} (\sigma_{N,i})^2} = \sqrt{\sum_{i=2012}^{2024} N_{\text{exp}, i}} = \sqrt{N_{\text{exp, tot}}}. \tag{8}$$

with $N_{\text{exp}, i}$ being the expected value and $\sigma_{N,i}$ the respective uncertainty of year i of Table 1.

4.2 Discussion of the Probability Results

Figure 8 shows the expected and measured numbers of LOFAR event matches of Table 1 for the different years. It is clear that the numbers match for the years 2018 – 2020 since we did not find any matches or solar flare candidates in these years.
The measurement points of the years 2015 – 2016 as well as 2021 – 2024 are contained in the error interval of the expected values. We notice that there are more matches measured in the years 2012 – 2014 and 2017 than expected. The actual numbers in these years are more than $5\,\sigma$ bigger than the calculated ones. This can have multiple reasons. We assumed that the LOFAR events are evenly distributed over one year which is not the case due to LOFAR downtime. In reality, the LOFAR uptimes are more irregular than we assume in our calculation. At a time period of high activity of the sun, this has a great impact on the values, since we then either miss or detect the solar flares that happen at that time.
In addition to that, we often found multiple events during one specific flare. These events then counted each as a match. That occurrences may not be well "covered" in our probability distribution which could lower the expected values. A calculation per month would have been more precise, because of the irregular measurement times of LOFAR. In the time period of this thesis, this was, however, not possible.
It may be the case that LOFAR has dedicated solar observations when a flare happens. Then we would expect more LOFAR matches with daytime solar flares.
Furthermore, we have to take into account that not all matches that were actually found have to stem from the sun, but there can also be the coincidence of measuring for example a CR signal and then interpreting it as a solar flare match.
It is important to look at the threshold flux that was set for finding solar flare candidates with the GOES data. If we had picked a lower threshold, there would have been more flares considered and the number of matches would have been higher and vice versa.

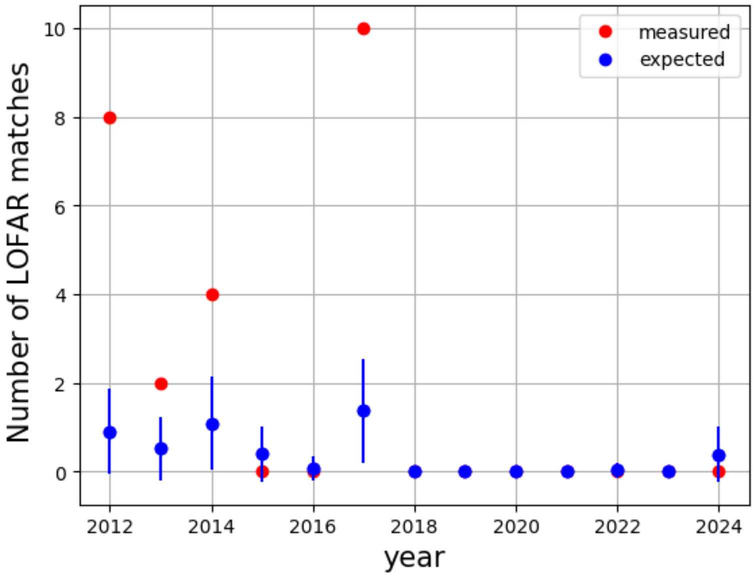

Figure 8: Expected and measured number of LOFAR event matches with solar flares during one specific year on daytime.

5 Identifying Solar Flares

In this chapter, all LOFAR event matches with solar flares during daytime will be examined. We made dynamic spectra plots, interferometric sky maps and looked for structures in the time domain data. For all the plots and data collection from LOFAR, the python framework NuRadioReco was used [29].

5.1 Searching for Solar Flares in LOFAR Data

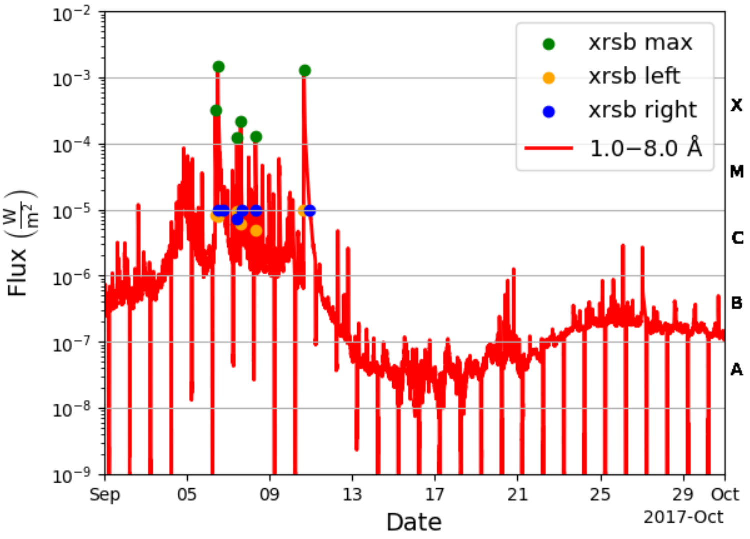

Figure 9: Plot of the measured flux over the time for september 2017 created with XRS-B data from the GOES satellites. The right axis shows the classification of each solar flare. The green points are the peaks above the threshold. The orange/blue points mark the beginning/stop of the flare.

As already explained in subsection 4.1, we used the data of the GOES satellites to search for the solar flares that happened during the years $2012 - 2024$. We set a threshold flux of $10^{-4}\,\frac{\mathrm{W}}{\mathrm{m}^2}$ for the peaks of the solar flares. With that, regarding the classification of solar flares (subsection 2.2), we limit the analysis to type X solar flares since this kind of flares create long-lasting radiation storms and have the highest peak strengths (cf. [12]). The condition for a solar flare to begin or stop was defined to be at the times when the measurement points meet an arbitrary threshold of $10^{-5}\,\frac{\mathrm{W}}{\mathrm{m}^2}$. An example plot for September 2017 is shown in Figure 9. Some data dropouts may occur during instrument calibrations or satellite eclipses when the earth or the moon is between the satellite and the sun, especially during spring and fall (cf. [30]). Since the minima in the plot happen in equidistant intervals once per day, the reason may be an eclipse.
We did not find any solar flare candidates for the years $2018 - 2020$. In 2016, only one possible solar flare happened (cf. Table 6), in 2021 only two (cf. Table 8). This has something to do with the solar cycle described in subsection 2.3. Compared to Figure 2, it makes sense that we did not measure any solar flares for $2018 - 2020$ since the activity of the Sun was at its minimum. 2016, the activity settled back to the minimum. In 2021, the activity began to increase again. We found 49 solar flare candidates for the

year 2024 since that was the year when the next solar cycle began (cf. Table 11 and Table 12).
Then we compared the LOFAR events to the flare times in those years. We found a number of matches with the solar flare candidates during daytime. These matches are listed in Table 13. Unfortunately, not all the LOFAR matches found were actually LBA events and our software does not allow to process HBA data currently. That is why only a part of the matches could be investigated. Now, the question is, if we actually see "something" in our LOFAR data.

5.2 Dynamic Spectra

In order to know if we actually see a solar flares structures in the LOFAR events that matched with solar flare times during daytime, we make dynamic spectra of these events.

5.2.1 Methods

We start with taking the raw signal (raw times, raw voltages). The voltage is a three-dimensional vector. We define the total voltage V_{total} as the sum of all components of the vector. Then we calculate

$$V = V_{\text{total}} - \langle \vec{V}_{\text{total}} \rangle \tag{9}$$

with $\langle \vec{V}_{\text{total}} \rangle$ being the mean value of the voltage components.
The sampling rate is 200 MHz. We bin our time and voltage values with a window width of 640 ns.
Then the x-axis values represent the mean time of each block. Moreover, we calculate the Discrete Fourier Transformation of the binned voltages to get the spectrum S:

$$S(f) = \sum_{n=0}^{N-1} V_{\text{binned}}(t) \cdot \exp\left(-i \cdot \frac{2\pi}{N} \cdot f \cdot t\right) \tag{10}$$

with $f = 0, .., N-1$. Then we determine the amplitude A by calculating the absolute value of $S(f)$.
Furthermore, we calculate the median M of the amplitude A over the time axis. The median over the time axis gives the typical noise spectrum per frequency.
Now we can divide the amplitude by the median to get the spectral excess above the median:

$$\text{Excess} = \frac{A}{M} \tag{11}$$

The excess clarifies how strong the signal is in comparison to the background.
Then, we transform the values into Decibels by using the following formula:

$$\text{Excess}\,[\text{dB}] = 20 \cdot \ln(\text{Excess}) \tag{12}$$

5.2.2 Discussion of the Results

We did not see anything noticeable in all the dynamic spectra except the one from 09/10/2017 at 15 : 55 : 33 UTC. All the other dynamic spectra are shown in subsection A.3. It has to be said that the time of recording the event is only a few minutes away from the peak of the flare (cf. Table 13). Figure 10 (a) shows the dynamic spectra of the event on 09/10/2017 at 15 : 55 : 33. Compared to a test event (b) of a CR, there is a broad signal visible that extends over the whole event at a frequency range of approximately $60 - 70\,\mathrm{MHz}$ which may be the solar flare.

The flare of September 10, 2017 was in fact the second largest flare of the solar cycle 24 (cf. [31]). The flare is also visible in Figure 9, which classifies it as a type X solar flare. The solar flare is associated with a very fast CME, talking about a velocity of $(3,038 \pm 288)\,\frac{\mathrm{km}}{\mathrm{s}}$. The flare and the CME happened at the western solar limb, looking at it from the perspective of the earth [31].

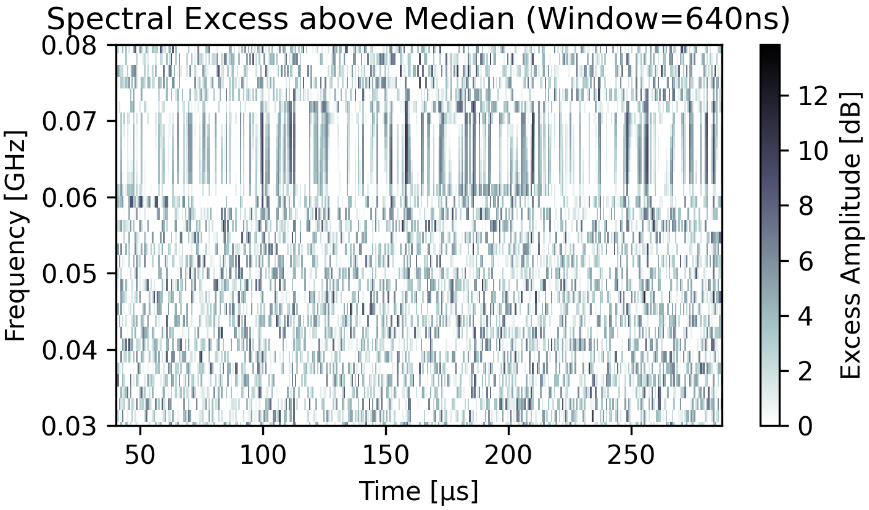

(a)

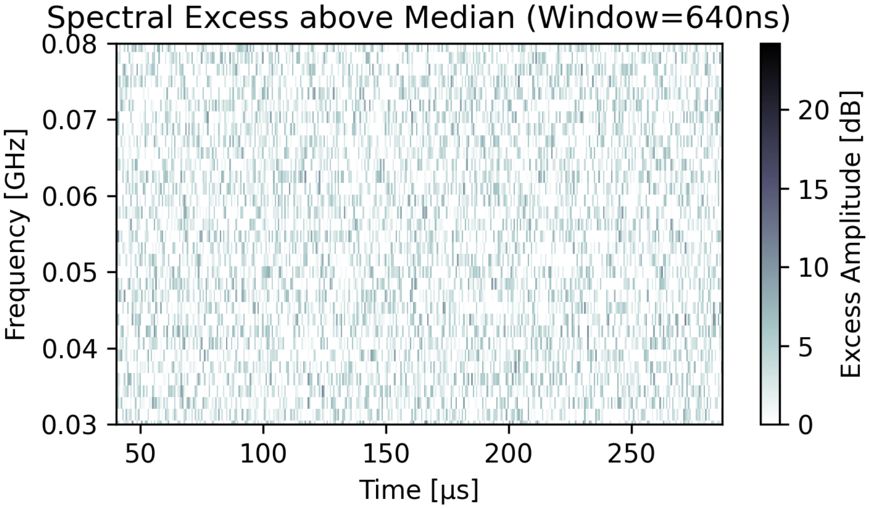

(b)

Figure 10: a) Dynamic spectrum plot based on the voltages of the LOFAR event on 09/10/2017 at 15 : 55 : 33 UTC. b) Test event (CR event) on 12/05/2012 at 05 : 16 : 44 UTC.

We also made a plot based on a sliding window view (cf. Figure 11). A sliding window slides across all dimensions of an array and extracts subsets of the array at all window positions. We chose a window size of 512 ns and a step size of 20 ns . Here, the possible solar flare signal and its limitation are better visible. It covers a frequency band of approximately 59 − 73 MHz. There are more structures observable, too. In a few of the structured regions, the spectral excess reaches up to approximately 12 dB.

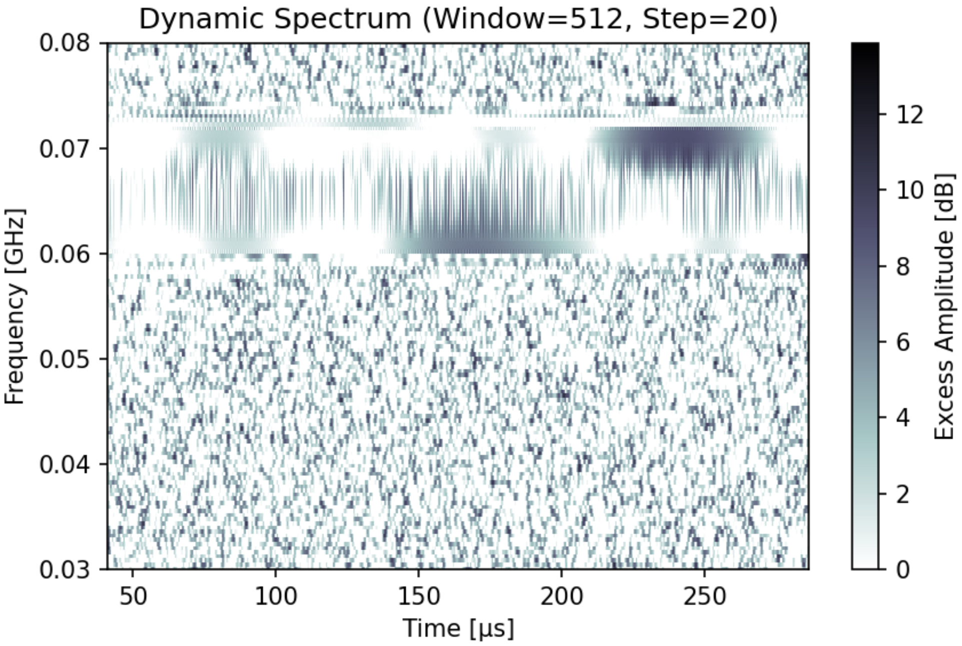

Figure 11: Dynamic spectrum plot with using a sliding window of the LOFAR event on 09/10/2017 at 15 : 55 : 33 UTC.

In order to be sure that our observations have something to do with the solar flare of 09/10/2017, we can compare it to the data of other observatories. The Royal Observatory of Belgium/HUMAIN collected some data about this flare and made a dynamic spectrum in a frequency band of 45 − 437 MHz (cf. Figure 12). There is a signal visible at approximately 50 − 80 MHz which would match our observation.
The e-Callisto in Austria-Unigraz also collected data and made a dynamic spectrum at a frequency band of 45 − 80 MHz which is suited better to compare with our data. They observed a really bright signal at around 15 : 55 UTC which matches exactly with our event (cf. Figure 13). This signal covers a frequency band of approximately 60 − 80 Mz which again goes perfectly with our data.
Finally, we can compare our data to the Irish and the core LOFAR station. Looking at the time of approximately 15 : 55 in Figure 14, it becomes apparent that the signal covers again a frequency band of about 55 − 80 MHz at that time. It was found that the majority of the observed radio emission of the flare consists of herringbones, among other radio structures. Moreover, three groups of herringbones were identified (cf. lower image in Figure 14). The first group of herringbones starts at 15 : 59 : 10 UT and covers a frequency range of 30 − 50 MHz. The herringbones themselves have a duration of up to 2 s. It contains the brightest shock signatures at low frequencies of the flare.

The second group of herringbones includes shorter herringbones (up to 1.5 s). The herringbones occur more frequently and in larger numbers compared to the first group, but the frequency range is the same. The third group shows the structure of a type II burst. It consists of two emission lanes, one at the fundamental (30 MHz) and one at the harmonic plasma frequency (60 MHz) [31].

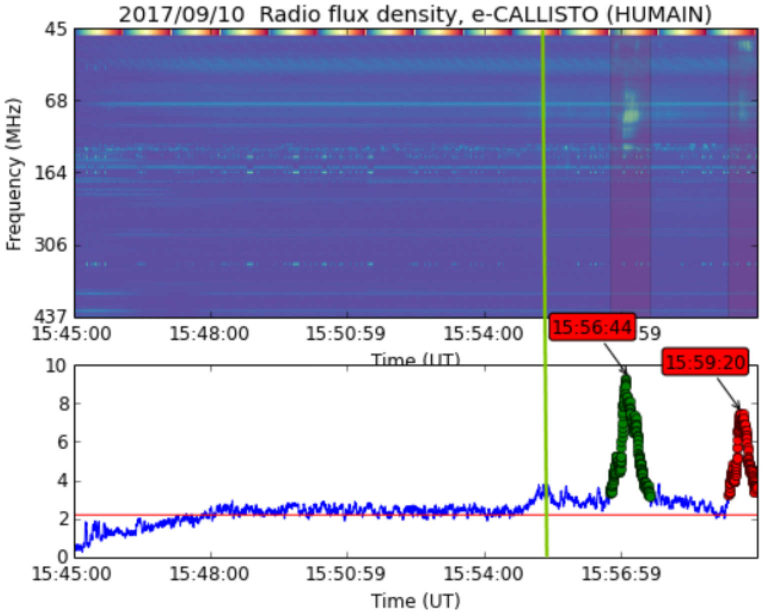

Figure 12: Dynamic spectrum of the Royal Observatory of Belgium/HUMAIN for the flare on 09/10/2017. The green line was added and represents the time of our LOFAR event on 09/10/2017 at 15 : 55 : 33 UTC. Figure adapted from [32].

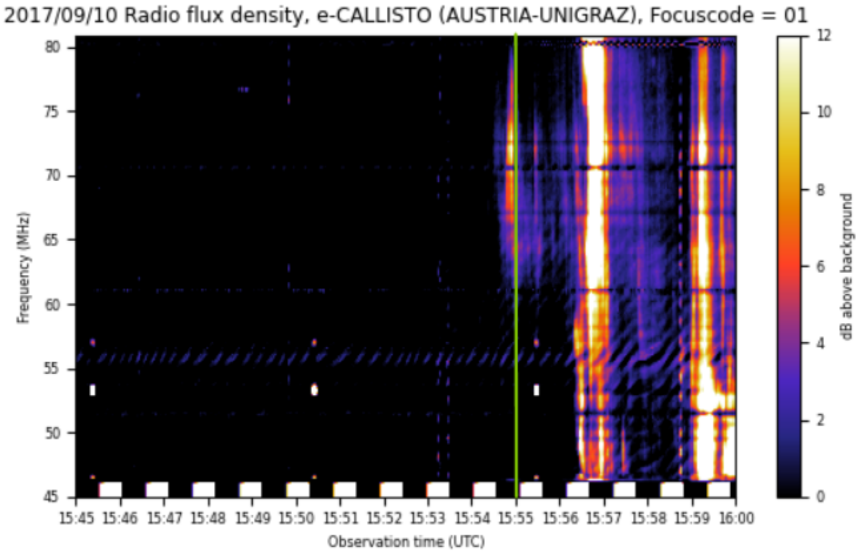

Figure 13: Dynamic spectrum plot of the e-Callisto observatory in Austria-Unigraz for the flare on 09/10/2017. The green line was added and represents the time of our LOFAR event on 09/10/2017 at 15 : 55 : 33 UTC. Figure adapted from [33].

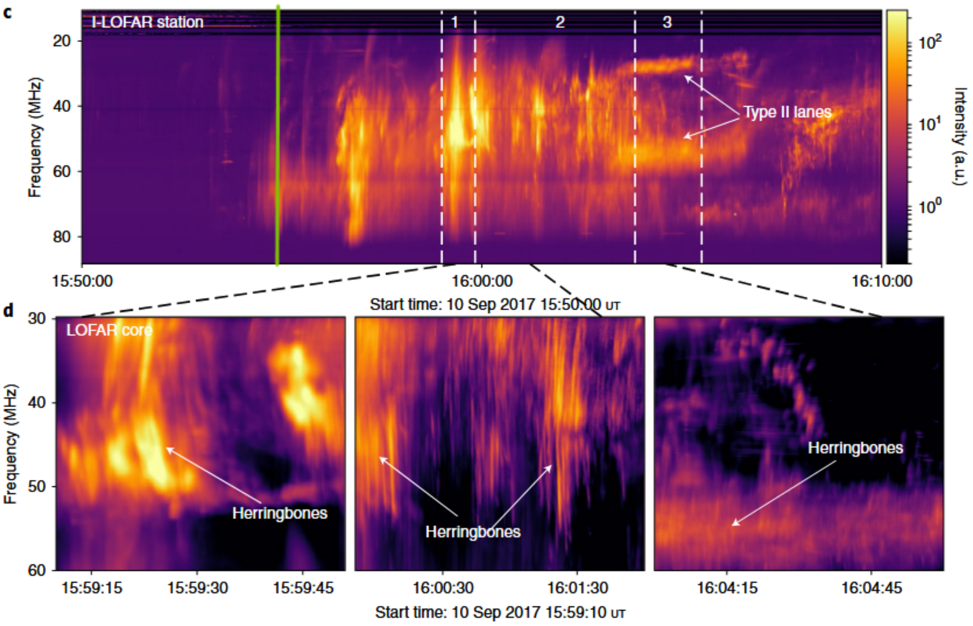

Figure 14: The upper figure shows the dynamic spectrum of the Irish LOFAR station for the flare on 09/10/2017. The lower figure shows high-resolution LOFAR core dynamic spectra of the fine-structured radio shock signatures called herringbones. The green line was added and represents the time of our LOFAR event on 09/10/2017 at $15:55:33$ UTC. Figure adapted from [31].

5.3 Interferometric Sky Map

It is important to know now if the signals of the LOFAR events actually stem from the sun. Therefore, we use interferometric sky maps. For the creation of the interferometric sky maps, the NuRadioReco beamformer module was used ([34], [35]).

5.3.1 Methods

We start with defining our coordinate system. The number of all antennas is N. The position of the n-th antenna is given by the vector:

$$\vec{r_{\mathrm{n}}} = (x_n, y_n, z_n) \tag{13}$$

These coordinates are defined relatively to the center of the station.
Now we need a unit direction vector that points at a certain point in the sky:

$$\vec{s} = \begin{pmatrix} \sin\theta \cdot \cos\phi \\ \sin\theta \cdot \sin\phi \\ \cos\theta \end{pmatrix} \tag{14}$$

ϕ is the azimuthal angle and θ is the zenith angle ($0\,^\circ$ mean vertically upwards).
We assume that the signal of the solar flare propagates as a plane wave signal. Due to the spatially distributed antennas, there is a geometric delay. That means that the signal reaches antenna A earlier than antenna B. The time delay can be calculated by dividing the additionally needed way for the signal to reach antenna n by the speed of light:

$$\tau_n(\vec{s}) = \frac{\vec{r_n} \cdot \vec{s}}{c}. \tag{15}$$

Next, we calculate the Fourier Transformation of the time series for each antenna:

$$x_n(t) \xrightarrow{\mathrm{FFT}} X_n(\nu) \tag{16}$$

A shift in time corresponds to a phase shift in the frequency. In order to shift our signal of antenna n in a way that it is in phase with our reference point, we multiply it by a phase factor ω_n:

$$\omega_n(\nu, \vec{s}) = \exp(-i \cdot 2\pi \cdot \nu \cdot \tau_n(\vec{s})) \tag{17}$$

Furthermore, we sum up all phase-corrected signals of all N antennas. The total signal for one specific frequency and one direction is then given by:

$$S(\nu, \vec{s}) = \sum_{n=1}^{N} X_n(\nu) \cdot \omega(\nu, \vec{s}) \tag{18}$$

If we look directly into the direction of the Sun and the signal stems from the Sun, the waves interfere constructively. Otherwise, destructive interference happens.
What we finally need is the intensity. Therefore, the power has to be calculated. We additionally sum over the frequency channels to suppress noise:

$$P(\vec{s}) = \sum_{\nu} |S(\nu, \vec{s})|^2. \tag{19}$$

5.3.2 Discussion of the Results

Figure 15 confirms that the signal of the LOFAR event on 09/10/2017 at 15 : 55 : 33 UTC actually came from the sun. The direction of the signal was identified to be at $\theta = 71.6\,^\circ$ and $\phi = 196.0\,^\circ$. The direction is the same for all stations (cf. Figure 16). The sky maps of Figure 15 and Figure 16 are made with a high resolution ($1\,^\circ$ resolution). We also created interferometric sky maps of the remaining LOFAR events which are listed in subsection A.4. These plots have been made with a lower resolution ($2\,^\circ$ resolution). The signals of 6 of the remaining 11 LOFAR events seem to stem from the sun, as the signals' peak position match the position of the Sun. Five of them belong to the same flare on 07/19/2012. Unfortunately, the dynamic spectra of these events do not show any structure, thus we cannot distinguish them from non-solar flare events. However, the sun can still be active without flaring, so we either just do not see a flare in our dynamic spectra and our frequency bandwidth or it may be another signal from the sun.

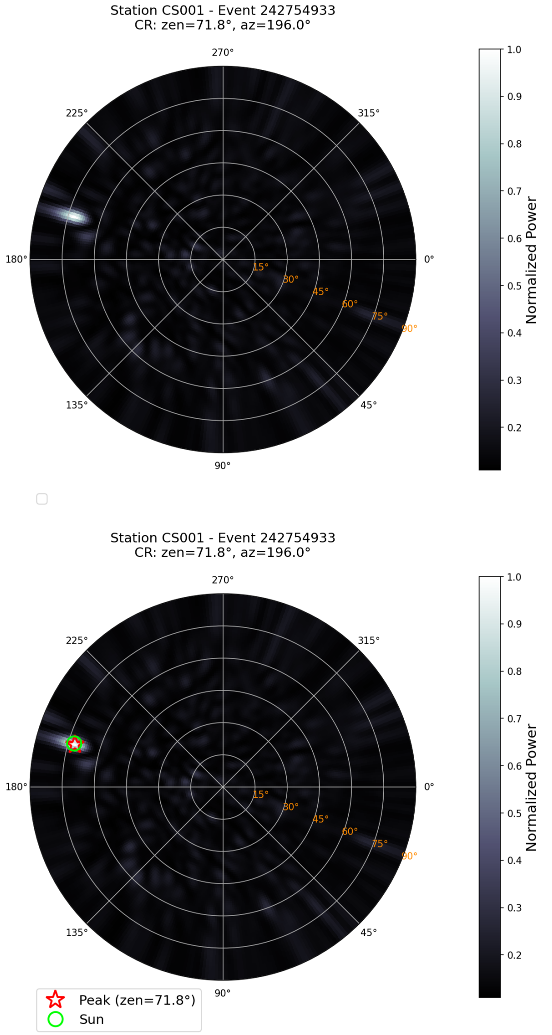

Figure 15: Interferometric sky map for station CS001 for the event on 09/10/2017. The position of the sun matches with the direction of the signal.

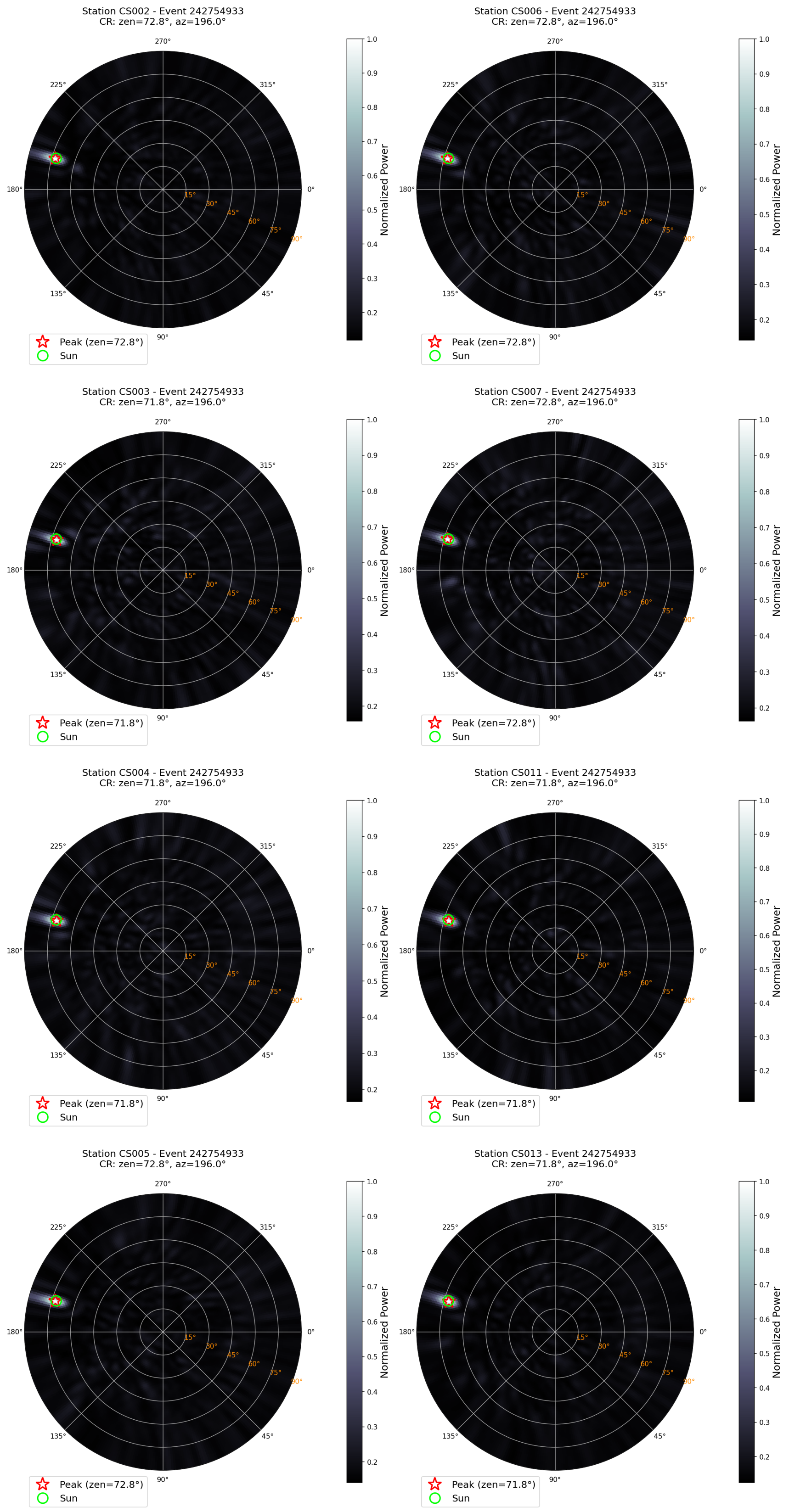

Figure 16: Remaining Interferometric sky maps for the other LOFAR stations of the LOFAR event on 09/10/2017 at $15:55:33$ UTC.

5.4 Time Domain

In this chapter, we want to look for structures in the time domain data of the LOFAR event on 09/10/2017 at 15 : 55 : 33 UTC.

5.4.1 Methods

The goal is to plot the beamformed time trace towards the peak direction. Therefore, we need to include the geometric delay of the antennas (explained in subsubsection 5.3.1). We calculate the beamformed spectrum as we do for the interferometric sky maps. Then we need to go back into the time domain. Therefore, we determine the inverse Fourier Transformation of the beamformed spectrum for each station to get the beamformed trace of the signal.

But we also need to include the geometric delay of the stations. This is the same principle as for the antennas, but on a wider scale (larger distances).

Then we can plot the beamformed trace over the time in ns.

In order to determine the correlation of the signals of different antennas or stations, we can take a look at the correlation function.

The cross-correlation function can be calculated with:

$$C_{x,y}(\tau) = \sum_{l=0}^{N-1} x_l(t) \cdot y^*_{l-k}(t) \tag{20}$$

with τ being a time delay between the two signals and $k = -(M-1), ..., (N-1)$, N is the length of x and M is the length of y. $x(t)$ and $y(t)$ are either the beamformed traces of station A and station B or the raw traces of antenna A and antenna B.

5.4.2 Discussion of the Results

Compared to a non-solar flare test-event, we note that the time domain data of the solar flare on 09/10/2017 at 15 : 55 : 33 UTC shows a "pulsed" structure (cf. Figure 18 and Figure 17). The remaining time domain plots of the other stations are shown in subsection A.5.

In order to know the exact correlation between our station signals, we calculate the cross - correlation function of the beamformed traces of station CS001 and station CS002. Figure 20 (a) shows that there is not much correlation between the signals. However, Figure 20 (b) reveals that the signals correlate more for the time delay that results from the geometric delay of the signal with respect to the Sun, since it lies on a side maxima of the correlation function.

We also calculated the cross-correlation function of the raw traces of one antenna of station CS001 and one antenna of station CS002. This again shows that the signals correlate more for the geometric delay of the antennas.

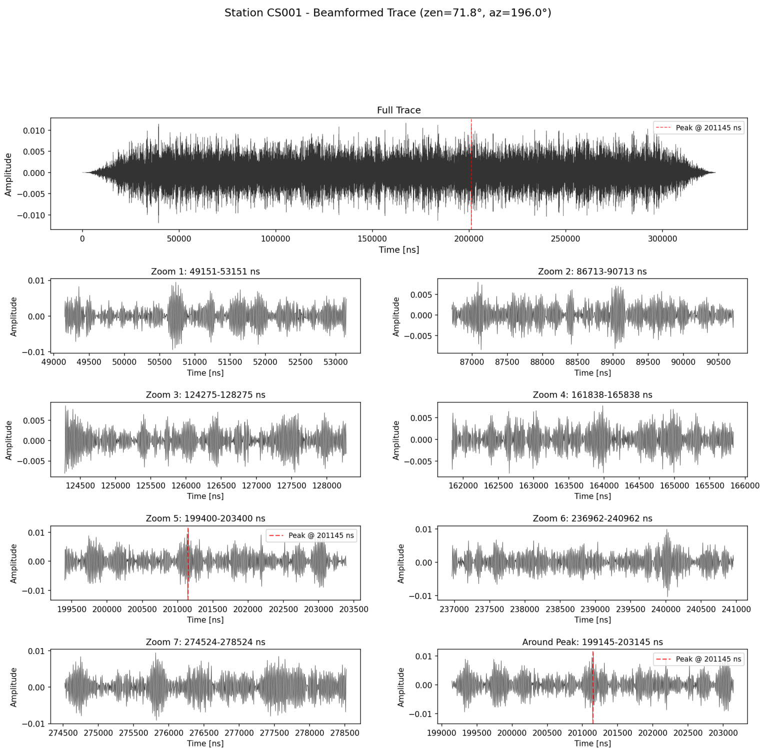

(a) Station CS001

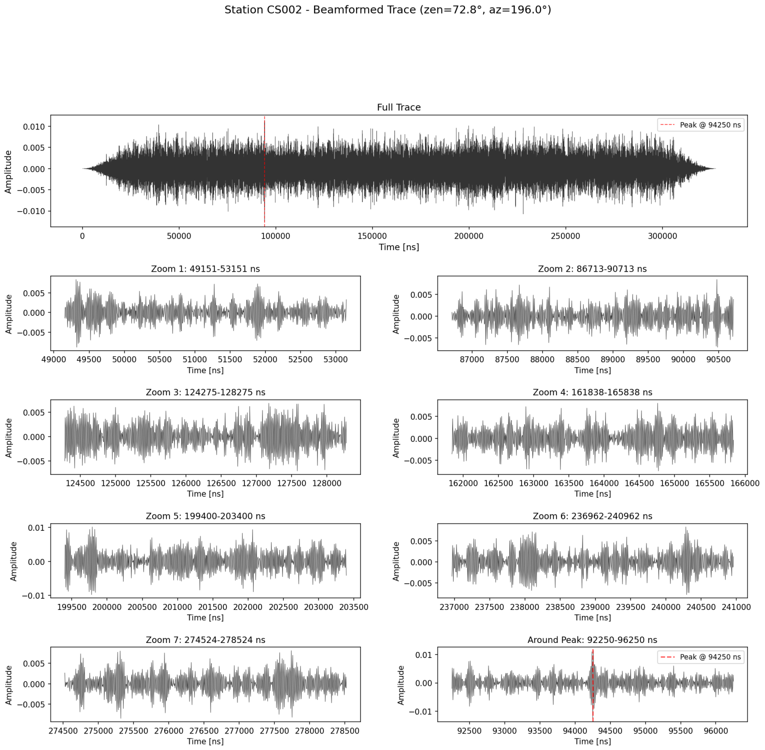

(b) Station CS002

Figure 17: Time domain plots of station CS001 and CS002 of the LOFAR event on 09/10/2017 at 15 : 55 : 33. There are additionally 7 ”zoom-ins” of the data and one around the peak of the data which is marked in red.

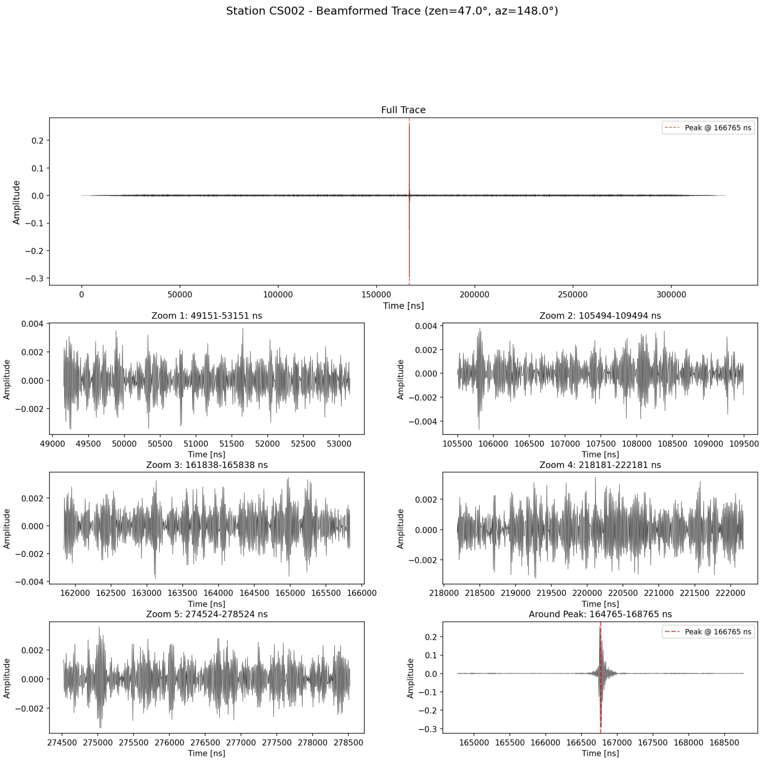

Figure 18: Plot of the time-domain data of a test event (CR event) on 12/05/2012 at 05 : 16 : 44 UTC.

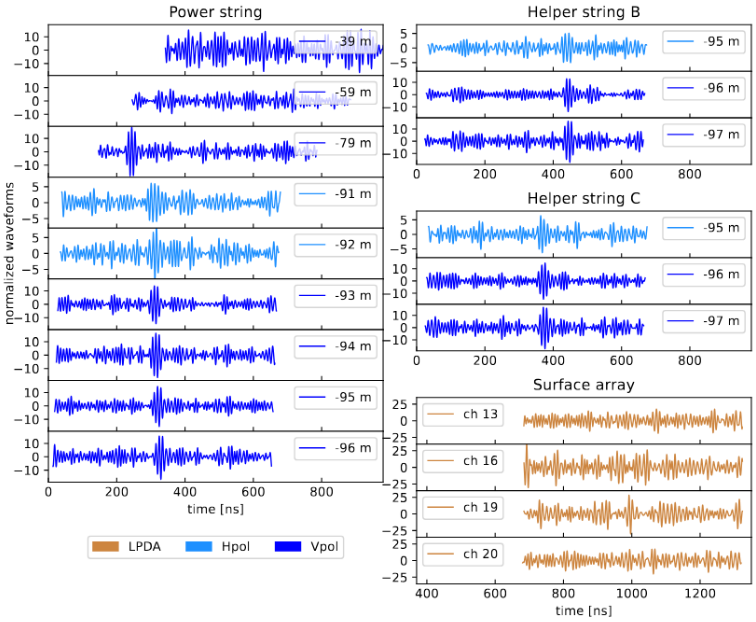

Figure 19: Waveforms for one event recorded in RNO-G during the September 29, 2022 solar flare. Figure taken from [11].

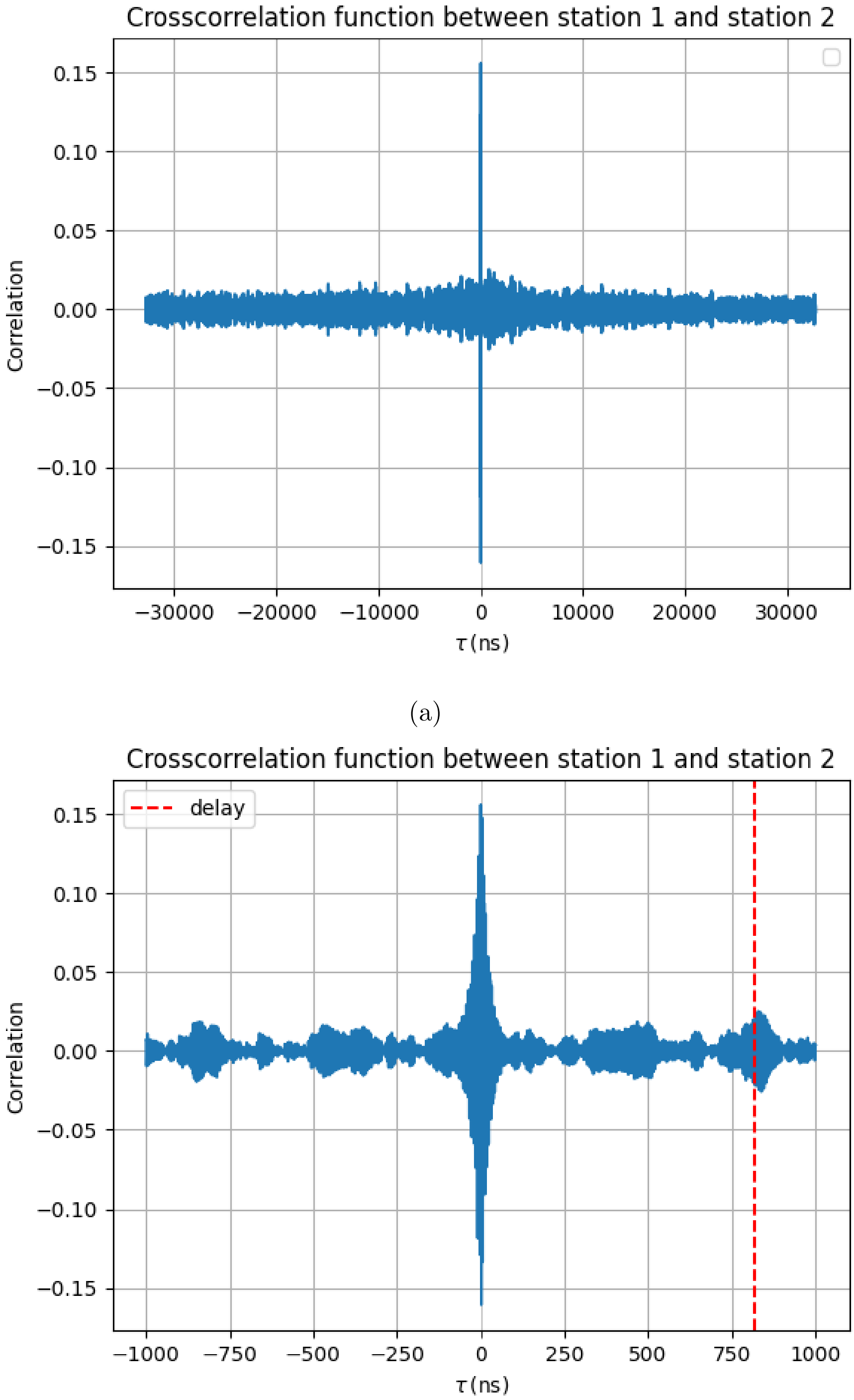

(a)

(b)

Figure 20: Calculated cross-correlation function of the beamformed traces of station CS001 and CS002. (a) shows the entire cross-correlation function, (b) shows a selected part of it. The red line is the geometric delay of the two stations with regard to the Sun.

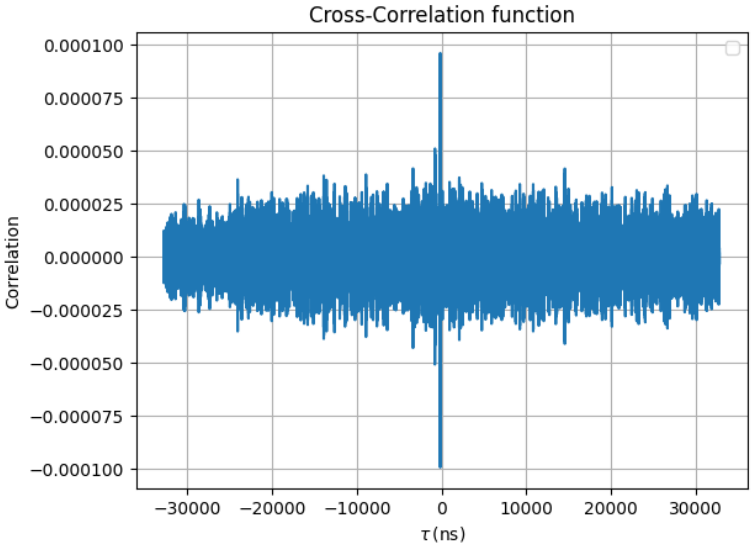

(a)

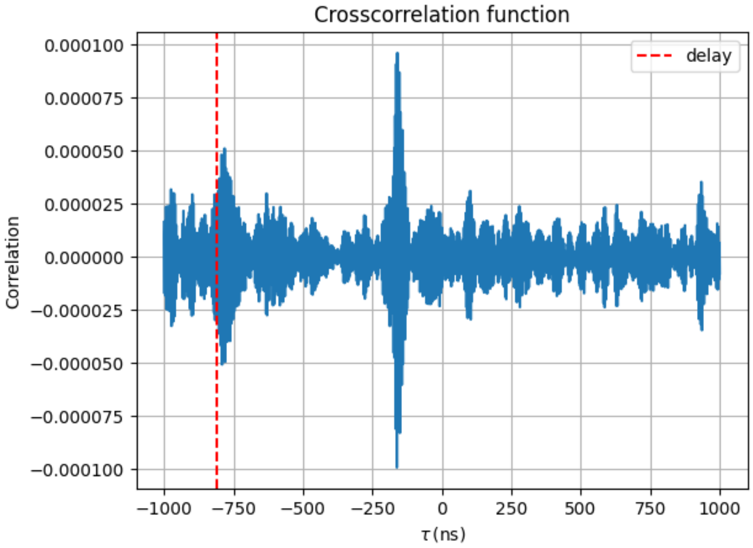

(b)

Figure 21: Calculated cross-correlation function of the raw traces of one antenna in station CS001 and one antenna in station CS002. (a) shows the entire cross-correlation function, (b) shows a selected part of it. The red line is the geometric delay of the two antennas with regard to the Sun.

In [11], it was found that recorded time-domain waveforms include among others, dispersive effects from the ionosphere. The waveforms show a high correlation (cf. Figure 19). For the low frequencies of RNO-G, dispersive delays across the band can add up to several tens to hundreds of nanoseconds, depending on the state of the ionosphere. We do not observe such a high correlation of the different LOFAR stations. The "pulsed" structure of our signals may result from antenna effects or have the same origin. This is, however, difficult to determine.

6 Conclusion

The goal of this thesis was to determine if we detected solar flares in the LOFAR CR mode in the years $2012 - 2024$. Additionally, we wanted to determine the expectation of LOFAR-event-matches with solar flares and analyze possible solar flare detections.

We started with examining the data of the GOES satellites of the time period of $2012 - 2024$. Therefore, we searched for all the solar flare candidates that reached or surpassed a threshold flux of $10^{-4}\,\frac{\mathrm{W}}{\mathrm{m}^2}$. We did not find any solar flares for the years $2018 - 2020$ since the activity of the sun was at its minimum (cf. Figure 2). The number of solar flare candidates found in the other years also correlated with the activity of the Sun. We found 49 solar flare candidates for 2024 since the new solar cycle began in that year.

The next step was to determine the number of LOFAR-event-matches with the daytime solar flares of these years. We found that the number of expected LOFAR-event-matches is lower than the actual number of matches. It turned out, that there are various reasons for that. We assumed that the LOFAR events are evenly distributed over one year in our calculation. In reality, this is not the case. There may be dedicated solar observations with LOFAR which could explain a more than $5\,\sigma$ deviation of the actual numbers in comparison with the expected values. It has to be said that not all the found LOFAR matches did in fact stem from the Sun or show solar flare signatures. Furthermore, the choice of the threshold flux has a great influence on the expected values as well, since the number of solar flares at a lower threshold would be much higher.

It has to be mentioned that we could not use all the LOFAR-event-matches that were found for further data analysis, since not all were LBA events. After we found the LOFAR-event-matches, we made dynamic spectra of each event. We found only one event that showed solar flare structures - the LOFAR event on 09/10/2017 at $15:55:33$ UTC. In fact, this event was from the second largest solar flare in the solar cycle 24 (cf. [31]).

We compared the determined dynamic spectra of this event to data of other observatories such as the Callisto telescopes HUMAIN and the one in Austria/Unigraz, as well as to the data of the core and the Irish LOFAR station. We found that our data matched really well with the data from the other observatories.

Furthermore, we determined interferometric sky maps of all the found LOFAR-event-matches to determine the direction of the signals. Our event of 09/10/2017 at $15:55:33$ did in fact stem from the Sun, which proves together with the analysis of its dynamic spectrum, that we detected a solar flare in CR mode. Additionally, we found that the signal of 6 other LOFAR-event-matches stemmed from the Sun. Unfortunately, we are not able to distinguish them from non-solar flare events since they did not show any structure in the corresponding dynamic spectra.

Then, we examined the time domain data of our detected solar flare to look for any noticeable structures. We did in fact find a "pulsed" structure and a small correlation for the geometric delay between the different station or antenna signals. This was proven by the calculation of the cross-correlation function of the beamformed traces of two stations and of the raw traces of two antennas of different stations.

In conclusion, we can say that we detected one solar flare - the second largest flare of solar cycle 24 (cf. [31]) - while being in LOFAR CR mode in the last few years. This may have been a serendipitous detection. But looking at the fact that we could not use many of the LOFAR-event-matches with daytime solar flares due to the fact that they were no LBA events, this might change for the future. The upgrade LOFAR2.0 proposes to enable simultaneous measurements of LBA and HBA antennas. This would provide us with a much wider frequency band and would increase the energy range in which it is possible to measure (cf. [27]). In future work, this could be used to analyze new data in a much more detailed way.

Acronyms

Callisto Compound Astronomical Low frequency Low cost Instrument for Spectroscopy and Transportable Observatory.

CME Coronal Mass Ejection.

CMEs Coronal Mass Ejections.

CR Cosmic Ray.

CRs Cosmic Rays.

FoV Field of View.

GOES Geostationary Operational Environmental Satellites.

GOES-XRS Geostationary Orbiting Environmental Satellites X-Ray Sensor.

HBA High-Band Antenna.

LBA Low-Band Antenna.

LNA Low-Noise Amplifier.

LOFAR LOw Frequency ARray.

LORA LOfar Radboud air shower Array.

NOAA National Oceanic and Atmospheric Administration.

PMTs Photo Multiplier Tubes.

RCUs Receiver Units.

RNO-G Radio Neutrino Observatory Greenland.

SEE Solar Eruptive Event.

TBB Transient Buffer Board.

A Appendix

A.1 Searching for Solar Flares with GOES

In the following tables, all solar flare candidates that were found between 2012 and 2024 with the GOES XRS-B data are listed.

Date	t_{begin}	t_{end}	t_{peak}	Flux of Peak $[\frac{\text{W}}{\text{m}^2}]$
01/23/2012	02 : 41 : 00	06 : 05 : 00	03 : 59 : 00	$1.26 \cdot 10^{-4}$
01/27/2012	18 : 09 : 00	20 : 54 : 00	18 : 37 : 00	$2.57 \cdot 10^{-4}$
03/05/2012	03 : 13 : 00	06 : 56 : 00	04 : 09 : 00	$1.64 \cdot 10^{-4}$
03/07/2012	00 : 05 : 00	04 : 02 : 00	00 : 24 : 00	$7.79 \cdot 10^{-4}$
03/10/2012	17 : 20 : 00	20 : 30 : 00	17 : 44 : 00	$1.22 \cdot 10^{-4}$
03/13/2012	17 : 16 : 00	20 : 25 : 00	17 : 41 : 00	$1.14 \cdot 10^{-4}$
07/06/2012	23 : 04 : 00	23 : 47 : 00	23 : 08 : 00	$1.61 \cdot 10^{-4}$
07/12/2012	16 : 14 : 00	20 : 00 : 00	16 : 52 : 00	$2.24 \cdot 10^{-4}$
07/19/2012	05 : 13 : 00	09 : 19 : 00	05 : 58 : 00	$1.12 \cdot 10^{-4}$
10/20/2012	18 : 09 : 00	18 : 36 : 00	18 : 14 : 00	$1.30 \cdot 10^{-4}$

Table 2: List of all solar flare candidates found in 2012 that are above a threshold flux of $10^{-4}\,\frac{\text{W}}{\text{m}^2}$. t_{begin} is the time when the solar flare began, t_{end} the time when it ended. t_{peak} represents the time when the flux was at its maximum. All times are UTC times.

Date	t_{begin}	t_{end}	t_{peak}	Flux of Peak $[\frac{\text{W}}{\text{m}^2}]$
05/13/2013	01 : 58 : 00	04 : 22 : 00	02 : 17 : 00	$2.51 \cdot 10^{-4}$
05/13/2013	15 : 51 : 00	18 : 09 : 00	16 : 05 : 00	$4.11 \cdot 10^{-4}$
05/14/2013	01 : 01 : 00	03 : 18 : 00	01 : 11 : 00	$4.64 \cdot 10^{-4}$
05/15/2013	01 : 30 : 00	03 : 31 : 00	01 : 48 : 00	$1.85 \cdot 10^{-4}$
10/24/2013	00 : 00 : 00	00 : 49 : 00	00 : 30 : 00	$1.34 \cdot 10^{-4}$
10/25/2013	07 : 56 : 00	08 : 59 : 00	08 : 01 : 00	$2.49 \cdot 10^{-4}$
10/25/2013	14 : 53 : 00	16 : 27 : 00	15 : 03 : 00	$3.05 \cdot 10^{-4}$
10/28/2013	01 : 45 : 00	02 : 39 : 00	02 : 03 : 00	$1.47 \cdot 10^{-4}$
10/29/2013	21 : 46 : 00	22 : 33 : 00	21 : 54 : 00	$3.37 \cdot 10^{-4}$
11/05/2013	22 : 10 : 00	22 : 23 : 00	22 : 12 : 00	$4.93 \cdot 10^{-4}$
11/08/2013	04 : 23 : 00	04 : 38 : 00	04 : 25 : 00	$1.62 \cdot 10^{-4}$
11/10/2013	05 : 10 : 00	05 : 30 : 00	05 : 14 : 00	$1.62 \cdot 10^{-4}$
11/19/2013	10 : 17 : 00	11 : 22 : 00	10 : 26 : 00	$1.49 \cdot 10^{-4}$

Table 3: List of all solar flare candidates found in 2013 that are above a threshold flux of $10^{-4}\,\frac{\text{W}}{\text{m}^2}$. t_{begin} is the time when the solar flare began, t_{end} the time when it ended. t_{peak} represents the time when the flux was at its maximum. All times are UTC times.

Date	t_{begin}	t_{end}	t_{peak}	Flux of Peak $[\frac{\text{W}}{\text{m}^2}]$
01/01/2014	18 : 44 : 00	21 : 18 : 00	18 : 52 : 00	$1.42 \cdot 10^{-4}$
01/07/2014	10 : 10 : 00	11 : 01 : 00	10 : 13 : 00	$1.04 \cdot 10^{-4}$
01/07/2014	18 : 09 : 00	20 : 05 : 00	18 : 32 : 00	$1.79 \cdot 10^{-4}$
02/25/2014	00 : 42 : 00	03 : 06 : 00	00 : 49 : 00	$7.13 \cdot 10^{-4}$
03/12/2014	22 : 31 : 00	23 : 21 : 00	22 : 34 : 00	$1.34 \cdot 10^{-4}$
03/29/2014	17 : 44 : 00	18 : 07 : 00	17 : 48 : 00	$1.45 \cdot 10^{-4}$
04/18/2014	12 : 45 : 00	13 : 49 : 00	13 : 03 : 00	$1.05 \cdot 10^{-4}$
04/25/2014	00 : 20 : 00	01 : 45 : 00	00 : 27 : 00	$1.99 \cdot 10^{-4}$
06/10/2014	11 : 39 : 00	11 : 52 : 00	11 : 42 : 00	$3.17 \cdot 10^{-4}$
06/10/2014	12 : 40 : 00	13 : 50 : 00	12 : 52 : 00	$2.22 \cdot 10^{-4}$
06/11/2014	09 : 01 : 00	09 : 23 : 00	09 : 06 : 00	$1.43 \cdot 10^{-4}$
09/10/2014	17 : 24 : 00	21 : 11 : 00	17 : 45 : 00	$2.39 \cdot 10^{-4}$
10/02/2014	17 : 29 : 00	19 : 45 : 00	19 : 01 : 00	$1.05 \cdot 10^{-4}$
10/19/2014	04 : 18 : 00	07 : 39 : 00	05 : 03 : 00	$1.58 \cdot 10^{-4}$
10/22/2014	01 : 31 : 00	03 : 25 : 00	01 : 59 : 00	$1.26 \cdot 10^{-4}$
10/22/2014	14 : 05 : 00	16 : 12 : 00	14 : 28 : 00	$2.39 \cdot 10^{-4}$
10/24/2014	21 : 08 : 00	23 : 59 : 00	21 : 41 : 00	$4.59 \cdot 10^{-4}$
10/25/2014	16 : 29 : 00	19 : 38 : 00	17 : 08 : 00	$1.50 \cdot 10^{-4}$
10/26/2014	10 : 36 : 00	12 : 27 : 00	10 : 56 : 00	$2.88 \cdot 10^{-4}$
10/27/2014	00 : 07 : 00	01 : 00 : 00	00 : 34 : 00	$1.03 \cdot 10^{-4}$
10/27/2014	14 : 16 : 00	16 : 36 : 00	14 : 47 : 00	$2.96 \cdot 10^{-4}$
11/05/2014	09 : 40 : 00	10 : 12 : 00	09 : 47 : 00	$1.14 \cdot 10^{-4}$
11/07/2014	16 : 56 : 00	19 : 16 : 00	17 : 25 : 00	$2.30 \cdot 10^{-4}$
12/17/2014	04 : 30 : 00	06 : 25 : 00	04 : 51 : 00	$1.25 \cdot 10^{-4}$
12/20/2014	00 : 15 : 00	04 : 13 : 00	00 : 27 : 00	$2.70 \cdot 10^{-4}$

Table 4: List of all solar flare candidates found in 2014 that are above a threshold flux of $10^{-4}\,\frac{\text{W}}{\text{m}^2}$. t_{begin} is the time when the solar flare began, t_{end} the time when it ended. t_{peak} represents the time when the flux was at its maximum. All times are UTC times.

Date	t_{begin}	t_{end}	t_{peak}	Flux of Peak $[\frac{\text{W}}{\text{m}^2}]$
03/03/2015	01 : 28 : 00	02 : 06 : 00	01 : 35 : 00	$1.18 \cdot 10^{-4}$
03/07/2015	21 : 57 : 00	23 : 59 : 00	22 : 22 : 00	$1.33 \cdot 10^{-4}$
03/11/2015	16 : 15 : 00	17 : 11 : 00	16 : 21 : 00	$3.15 \cdot 10^{-4}$
05/05/2015	22 : 07 : 00	22 : 37 : 00	22 : 11 : 00	$3.93 \cdot 10^{-4}$
06/26/2015	08 : 11 : 00	11 : 00 : 00	08 : 16 : 00	$1.13 \cdot 10^{-4}$
09/28/2015	14 : 54 : 00	15 : 25 : 00	14 : 58 : 00	$1.09 \cdot 10^{-4}$

Table 5: List of all solar flare candidates found in 2015 that are above a threshold flux of $10^{-4}\,\frac{\text{W}}{\text{m}^2}$. t_{begin} is the time when the solar flare began, t_{end} the time when it ended. t_{peak} represents the time when the flux was at its maximum. All times are UTC times.

Date	t_{begin}	t_{end}	t_{peak}	Flux of Peak $[\frac{\text{W}}{\text{m}^2}]$
07/23/2016	05 : 10 : 00	05 : 51 : 00	05 : 16 : 00	$1.09 \cdot 10^{-4}$

Table 6: Solar flare candidate that was found in 2016 above a threshold flux of $10^{-4}\,\frac{\text{W}}{\text{m}^2}$. t_{begin} is the time when the solar flare began, t_{end} the time when it ended. t_{peak} represents the time when the flux was at its maximum. All times are UTC times.

Date	t_{begin}	t_{end}	t_{peak}	Flux of Peak $[\frac{\text{W}}{\text{m}^2}]$
09/06/2017	09 : 20 : 00	11 : 35 : 00	09 : 27 : 00	$1.10 \cdot 10^{-4}$
09/06/2017	11 : 53 : 00	18 : 09 : 00	12 : 02 : 00	$1.34 \cdot 10^{-3}$
09/07/2017	10 : 14 : 00	10 : 23 : 00	10 : 15 : 00	$1.09 \cdot 10^{-4}$
09/07/2017	14 : 31 : 00	15 : 58 : 00	14 : 36 : 00	$1.99 \cdot 10^{-4}$
09/08/2017	07 : 44 : 00	08 : 30 : 00	07 : 49 : 00	$1.16 \cdot 10^{-4}$
09/10/2017	15 : 47 : 00	22 : 32 : 00	16 : 06 : 00	$1.19 \cdot 10^{-3}$

Table 7: List of all solar flare candidates found in 2017 that are above a threshold flux of $10^{-4}\,\frac{\text{W}}{\text{m}^2}$. t_{begin} is the time when the solar flare began, t_{end} the time when it ended. t_{peak} represents the time when the flux was at its maximum. All times are UTC times.

Date	t_{begin}	t_{end}	t_{peak}	Flux of Peak $[\frac{\text{W}}{\text{m}^2}]$
07/03/2021	14 : 26 : 00	14 : 42 : 00	14 : 29 : 00	$1.59 \cdot 10^{-4}$
10/28/2021	15 : 27 : 00	16 : 26 : 00	15 : 35 : 00	$1.00 \cdot 10^{-4}$

Table 8: Solar flare candiates found in 2021 that are above a threshold flux of $10^{-4}\,\frac{\text{W}}{\text{m}^2}$. t_{begin} is the time when the solar flare began, t_{end} the time when it ended. t_{peak} represents the time when the flux was at its maximum. All times are UTC times.

Date	t_{begin}	t_{end}	t_{peak}	Flux of Peak $[\frac{\text{W}}{\text{m}^2}]$
03/30/2022	17 : 29 : 00	18 : 20 : 00	17 : 37 : 00	$1.38 \cdot 10^{-4}$
04/17/2022	03 : 24 : 00	05 : 04 : 00	03 : 34 : 00	$1.17 \cdot 10^{-4}$
04/20/2022	03 : 52 : 00	04 : 16 : 00	03 : 57 : 00	$2.25 \cdot 10^{-4}$
04/30/2022	13 : 42 : 00	13 : 55 : 00	13 : 47 : 00	$1.13 \cdot 10^{-4}$
05/03/2022	13 : 21 : 00	13 : 45 : 00	13 : 25 : 00	$1.13 \cdot 10^{-4}$
05/10/2022	13 : 53 : 00	14 : 06 : 00	13 : 55 : 00	$1.51 \cdot 10^{-4}$
10/02/2022	20 : 04 : 00	20 : 59 : 00	20 : 25 : 00	$1.06 \cdot 10^{-4}$

Table 9: List of all solar flare candiates found in 2022 that are above a threshold flux of $10^{-4}\,\frac{\text{W}}{\text{m}^2}$. t_{begin} is the time when the solar flare began, t_{end} the time when it ended. t_{peak} represents the time when the flux was at its maximum. All times are UTC times.

Date	t_{begin}	t_{end}	t_{peak}	Flux of Peak $[\frac{\text{W}}{\text{m}^2}]$
01/06/2023	$00:54:00$	$01:51:00$	$00:57:00$	$1.22 \cdot 10^{-4}$
01/09/2023	$18:44:00$	$19:19:00$	$18:50:00$	$1.98 \cdot 10^{-4}$
01/10/2023	$22:45:00$	$22:55:00$	$22:47:00$	$1.06 \cdot 10^{-4}$
02/11/2023	$15:44:00$	$16:06:00$	$15:48:00$	$1.16 \cdot 10^{-4}$
02/17/2023	$19:55:00$	$23:59:00$	$20:16:00$	$2.28 \cdot 10^{-4}$
03/03/2023	$17:48:00$	$18:53:00$	$17:52:00$	$2.07 \cdot 10^{-4}$
03/29/2023	$02:29:00$	$03:03:00$	$02:33:00$	$1.27 \cdot 10^{-4}$
07/02/2023	$23:02:00$	$23:59:00$	$23:14:00$	$1.07 \cdot 10^{-4}$
08/05/2023	$21:57:00$	$23:59:00$	$22:21:00$	$1.62 \cdot 10^{-4}$
08/07/2023	$20:34:00$	$22:44:00$	$20:46:00$	$1.50 \cdot 10^{-4}$
12/14/2023	$16:55:00$	$19:20:00$	$17:02:00$	$2.84 \cdot 10^{-4}$
12/31/2023	$21:38:00$	$23:28:00$	$21:55:00$	$4.96 \cdot 10^{-4}$

Table 10: List of all solar flare candidates found in 2023 that are above a threshold flux of $10^{-4}\,\frac{\text{W}}{\text{m}^2}$. t_{begin} is the time when the solar flare began, t_{end} the time when it ended. t_{peak} represents the time when the flux was at its maximum. All times are UTC times.

Date	t_{begin}	t_{end}	t_{peak}	Flux of Peak $[\frac{\mathrm{W}}{\mathrm{m}^2}]$
02/09/2024	12 : 59 : 00	15 : 43 : 00	13 : 14 : 00	$3.35 \cdot 10^{-4}$
02/16/2024	06 : 49 : 00	07 : 06 : 00	06 : 53 : 00	$2.53 \cdot 10^{-4}$
02/21/2024	22 : 59 : 00	23 : 39 : 00	23 : 07 : 00	$1.88 \cdot 10^{-4}$
02/22/2024	06 : 27 : 00	07 : 37 : 00	06 : 32 : 00	$1.69 \cdot 10^{-4}$
03/23/2024	01 : 07 : 00	04 : 32 : 00	01 : 33 : 00	$1.11 \cdot 10^{-4}$
03/28/2024	20 : 36 : 00	21 : 47 : 00	20 : 56 : 00	$1.11 \cdot 10^{-4}$
05/05/2024	05 : 54 : 00	06 : 45 : 00	06 : 01 : 00	$1.31 \cdot 10^{-4}$
05/05/2024	11 : 43 : 00	13 : 13 : 00	11 : 54 : 00	$1.28 \cdot 10^{-4}$
05/06/2024	05 : 18 : 00	08 : 41 : 00	06 : 35 : 00	$4.47 \cdot 10^{-4}$
05/08/2024	01 : 37 : 00	01 : 58 : 00	01 : 41 : 00	$1.07 \cdot 10^{-4}$
05/08/2024	03 : 15 : 00	13 : 47 : 00	05 : 09 : 00	$1.03 \cdot 10^{-4}$
05/08/2024	21 : 04 : 00	23 : 59 : 00	21 : 40 : 00	$1.01 \cdot 10^{-4}$
05/09/2024	08 : 23 : 00	11 : 32 : 00	09 : 13 : 00	$2.23 \cdot 10^{-4}$
05/09/2024	17 : 42 : 00	19 : 46 : 00	17 : 44 : 00	$1.11 \cdot 10^{-4}$
05/10/2024	06 : 19 : 00	10 : 52 : 00	06 : 54 : 00	$3.94 \cdot 10^{-4}$
05/11/2024	01 : 10 : 00	03 : 21 : 00	01 : 23 : 00	$5.83 \cdot 10^{-4}$
05/11/2024	11 : 11 : 00	13 : 41 : 00	11 : 44 : 00	$1.52 \cdot 10^{-4}$
05/12/2024	16 : 14 : 00	16 : 57 : 00	16 : 26 : 00	$1.01 \cdot 10^{-4}$
05/14/2024	01 : 33 : 00	03 : 12 : 00	02 : 09 : 00	$1.70 \cdot 10^{-4}$
05/14/2024	12 : 45 : 00	13 : 29 : 00	12 : 55 : 00	$1.24 \cdot 10^{-4}$
05/14/2024	16 : 46 : 00	20 : 18 : 00	16 : 51 : 00	$8.71 \cdot 10^{-4}$
05/15/2024	08 : 21 : 00	16 : 45 : 00	08 : 37 : 00	$3.45 \cdot 10^{-4}$
05/15/2024	08 : 21 : 00	16 : 45 : 00	14 : 38 : 00	$2.96 \cdot 10^{-4}$
05/27/2024	06 : 57 : 00	10 : 00 : 00	07 : 08 : 00	$2.87 \cdot 10^{-4}$
05/29/2024	14 : 04 : 00	19 : 20 : 00	14 : 37 : 00	$1.43 \cdot 10^{-4}$
05/31/2024	21 : 59 : 00	22 : 35 : 00	22 : 03 : 00	$1.17 \cdot 10^{-4}$
06/01/2024	08 : 42 : 00	09 : 50 : 00	08 : 48 : 00	$1.41 \cdot 10^{-4}$
06/01/2024	18 : 31 : 00	21 : 53 : 00	18 : 36 : 00	$1.02 \cdot 10^{-4}$
06/10/2024	09 : 47 : 00	12 : 26 : 00	11 : 08 : 00	$1.54 \cdot 10^{-4}$
07/14/2024	02 : 28 : 00	03 : 41 : 00	02 : 34 : 00	$1.26 \cdot 10^{-4}$
07/16/2024	13 : 18 : 00	14 : 29 : 00	13 : 26 : 00	$1.98 \cdot 10^{-4}$
07/29/2024	02 : 32 : 00	03 : 01 : 00	02 : 37 : 00	$1.55 \cdot 10^{-4}$
08/05/2024	13 : 28 : 00	15 : 13 : 00	13 : 40 : 00	$1.72 \cdot 10^{-4}$
08/05/2024	15 : 19 : 00	15 : 36 : 00	15 : 27 : 00	$1.16 \cdot 10^{-4}$
08/08/2024	19 : 18 : 00	20 : 55 : 00	19 : 35 : 00	$1.29 \cdot 10^{-4}$
08/14/2024	06 : 06 : 00	08 : 01 : 00	06 : 40 : 00	$1.10 \cdot 10^{-4}$

Table 11: List of all solar flare candidates found in 2024 until the end of august that are above a threshold flux of $10^{-4}\,\frac{\mathrm{W}}{\mathrm{m}^2}$. t_{begin} is the time when the solar flare began, t_{end} the time when it ended. t_{peak} represents the time when the flux was at its maximum. All times are UTC times.

Date	t_{begin}	t_{end}	t_{peak}	Flux of Peak $[\frac{\text{W}}{\text{m}^2}]$
09/12/2024	09 : 36 : 00	10 : 34 : 00	09 : 43 : 00	$1.29 \cdot 10^{-4}$
09/14/2024	15 : 16 : 00	18 : 01 : 00	15 : 29 : 00	$4.49 \cdot 10^{-4}$
10/01/2024	22 : 07 : 00	23 : 45 : 00	22 : 20 : 00	$7.08 \cdot 10^{-4}$
10/03/2024	12 : 12 : 00	18 : 02 : 00	12 : 18 : 00	$8.96 \cdot 10^{-4}$
10/07/2024	18 : 18 : 00	23 : 59 : 00	19 : 13 : 00	$2.17 \cdot 10^{-4}$
10/09/2024	01 : 35 : 00	04 : 23 : 00	01 : 56 : 00	$1.83 \cdot 10^{-4}$
10/09/2024	15 : 44 : 00	16 : 00 : 00	15 : 47 : 00	$1.42 \cdot 10^{-4}$
10/24/2024	03 : 38 : 00	08 : 50 : 00	03 : 57 : 00	$3.30 \cdot 10^{-4}$
10/26/2024	06 : 02 : 00	13 : 42 : 00	07 : 19 : 00	$1.85 \cdot 10^{-4}$
10/31/2024	21 : 07 : 00	23 : 21 : 00	21 : 20 : 00	$2.01 \cdot 10^{-4}$
11/06/2024	13 : 31 : 00	16 : 17 : 00	13 : 40 : 00	$2.37 \cdot 10^{-4}$
12/08/2024	09 : 01 : 00	09 : 25 : 00	09 : 06 : 00	$2.27 \cdot 10^{-4}$
12/29/2024	04 : 18 : 00	11 : 35 : 00	07 : 17 : 00	$1.13 \cdot 10^{-4}$

Table 12: List of all solar flare candidates found from september 2024 until the end of 2024 that are above a threshold flux of $10^{-4}\,\frac{\text{W}}{\text{m}^2}$. t_{begin} is the time when the solar flare began, t_{end} the time when it ended. t_{peak} represents the time when the flux was at its maximum. All times are UTC times.

A.2 LOFAR matches

Date	t_{lofar}	t_{begin}	t_{end}	t_{peak}	Flux of Peak $[\frac{\text{W}}{\text{m}^2}]$
07/19/2012	**05 : 27 : 12**	05 : 13 : 00	09 : 19 : 00	05 : 58 : 00	$1.12 \cdot 10^{-4}$
07/19/2012	**05 : 35 : 18**	05 : 13 : 00	09 : 19 : 00	05 : 58 : 00	$1.12 \cdot 10^{-4}$
07/19/2012	05 : 36 : 48	05 : 13 : 00	09 : 19 : 00	05 : 58 : 00	$1.12 \cdot 10^{-4}$
07/19/2012	05 : 42 : 32	05 : 13 : 00	09 : 19 : 00	05 : 58 : 00	$1.12 \cdot 10^{-4}$
07/19/2012	**05 : 57 : 04**	05 : 13 : 00	09 : 19 : 00	05 : 58 : 00	$1.12 \cdot 10^{-4}$
07/19/2012	**06 : 02 : 25**	05 : 13 : 00	09 : 19 : 00	05 : 58 : 00	$1.12 \cdot 10^{-4}$
07/19/2012	**06 : 14 : 20**	05 : 13 : 00	09 : 19 : 00	05 : 58 : 00	$1.12 \cdot 10^{-4}$
07/19/2012	06 : 17 : 33	05 : 13 : 00	09 : 19 : 00	05 : 58 : 00	$1.12 \cdot 10^{-4}$
10/25/2013	**15 : 27 : 59**	14 : 53 : 00	16 : 27 : 00	15 : 03 : 00	$3.05 \cdot 10^{-4}$
10/25/2013	15 : 51 : 39	14 : 53 : 00	16 : 27 : 00	15 : 03 : 00	$3.05 \cdot 10^{-4}$
10/19/2014	06 : 40 : 22	04 : 18 : 00	07 : 39 : 00	05 : 03 : 00	$1.58 \cdot 10^{-4}$
10/19/2014	**07 : 35 : 26**	04 : 18 : 00	07 : 39 : 00	05 : 03 : 00	$1.58 \cdot 10^{-4}$
10/22/2014	14 : 26 : 16	14 : 05 : 00	16 : 12 : 00	14 : 28 : 00	$2.39 \cdot 10^{-4}$
10/27/2014	14 : 24 : 32	14 : 16 : 00	16 : 36 : 00	14 : 47 : 00	$2.96 \cdot 10^{-4}$
09/06/2017	**12 : 07 : 10**	11 : 53 : 00	18 : 09 : 00	12 : 02 : 00	$1.34 \cdot 10^{-3}$
09/06/2017	**17 : 29 : 15**	11 : 53 : 00	18 : 09 : 00	12 : 02 : 00	$1.34 \cdot 10^{-3}$
09/06/2017	18 : 08 : 42	11 : 53 : 00	18 : 09 : 00	12 : 02 : 00	$1.34 \cdot 10^{-3}$
09/10/2017	**15 : 55 : 33**	15 : 47 : 00	22 : 32 : 00	16 : 06 : 00	$1.19 \cdot 10^{-3}$
09/10/2017	**16 : 48 : 18**	15 : 47 : 00	22 : 32 : 00	16 : 06 : 00	$1.19 \cdot 10^{-3}$
09/10/2017	**16 : 58 : 07**	15 : 47 : 00	22 : 32 : 00	16 : 06 : 00	$1.19 \cdot 10^{-3}$
09/10/2017	17 : 22 : 29	15 : 47 : 00	22 : 32 : 00	16 : 06 : 00	$1.19 \cdot 10^{-3}$
09/10/2017	18 : 27 : 40	15 : 47 : 00	22 : 32 : 00	16 : 06 : 00	$1.19 \cdot 10^{-3}$
09/10/2017	21 : 11 : 22	15 : 47 : 00	22 : 32 : 00	16 : 06 : 00	$1.19 \cdot 10^{-3}$
09/10/2017	22 : 05 : 38	15 : 47 : 00	22 : 32 : 00	16 : 06 : 00	$1.19 \cdot 10^{-3}$

Table 13: List of LOFAR matches found for 2012 − 2024 during daytime. t_{lofar} is the time of the LOFAR event. The associated solar flare candidates that are above a threshold flux of $10^{-4}\,\frac{\text{W}}{\text{m}^2}$ are listed next to the matches. t_{begin} is the time when the solar flare began, t_{end} the time when it ended. t_{peak} represents the time when the flux was at its maximum. All times are UTC times. Only the **marked** LOFAR events could be examined further.

A.3 Dynamic Spectra

The following figures show the dynamic spectra plots of the remaining LOFAR events. Unfortunately, there is no solar flare signal visible.

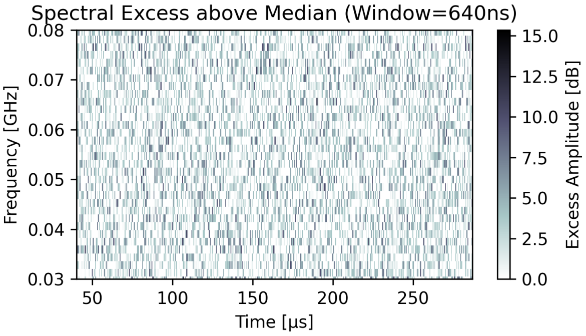
Spectral Excess above Median (Window=640ns)

(a) 05 : 27 : 12 UTC.

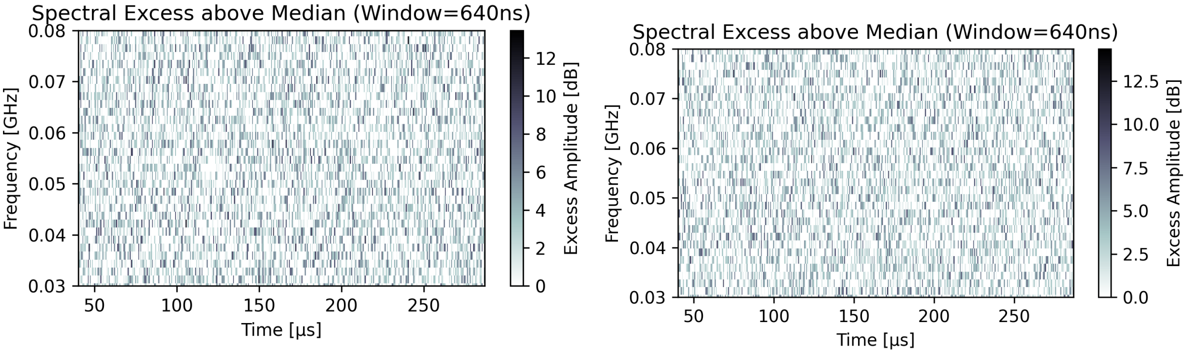
Spectral Excess above Median (Window=640ns)

Spectral Excess above Median (Window=640ns)

(b) 05 : 35 : 18 UTC.

(d) 05 : 57 : 04 UTC.

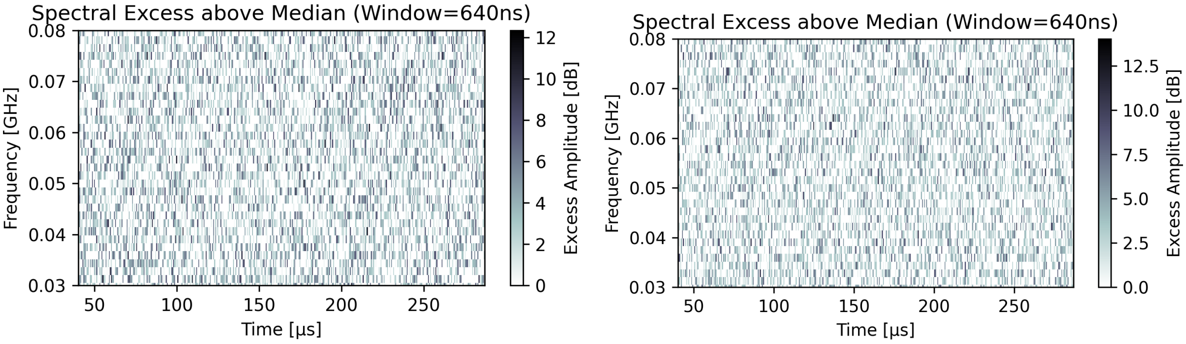
Spectral Excess above Median (Window=640ns)

Spectral Excess above Median (Window=640ns)

(c) 06 : 02 : 25 UTC.

(e) 06 : 14 : 20 UTC.

Figure 22: Dynamic spectra plots of the LOFAR events on 07/19/2012.

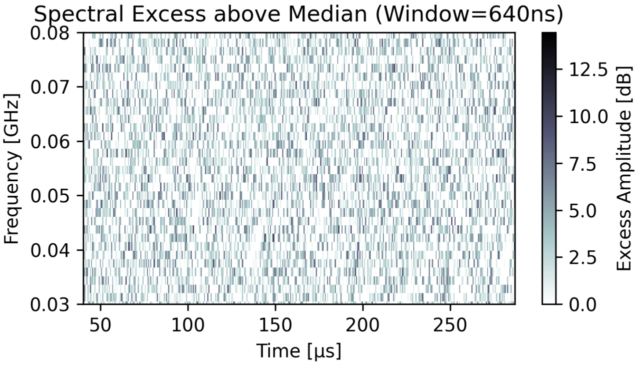

Figure 23: Dynamic spectrum plot of the LOFAR event on 10/25/2013 at 15 : 27 : 59 UTC.

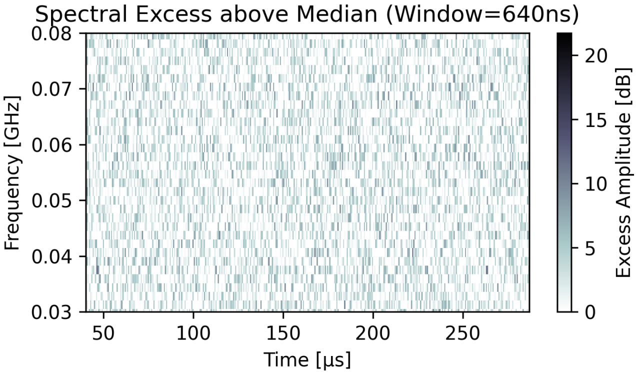

Figure 24: Dynamic spectrum plot of the LOFAR event on 10/19/2014 at 07 : 35 : 26 UTC.

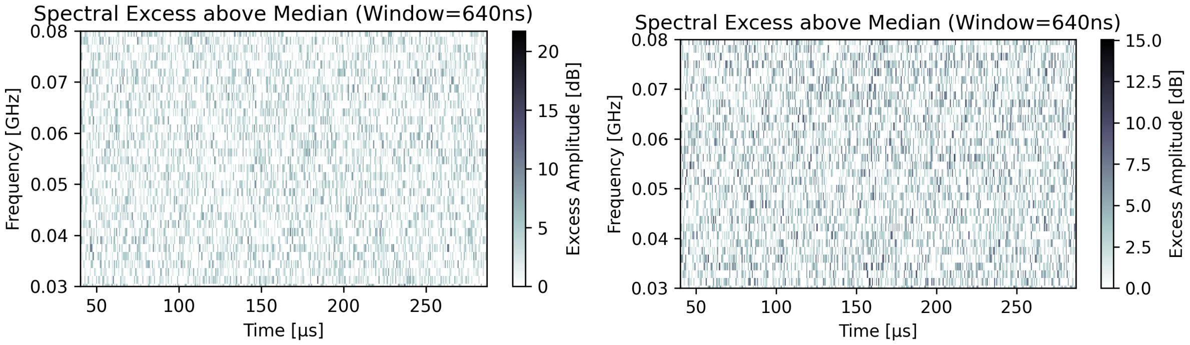

(a) 12 : 07 : 10 UTC.

(b) 17 : 29 : 15 UTC.

Figure 25: Dynamic spectra plots of the LOFAR events on 09/06/2017.

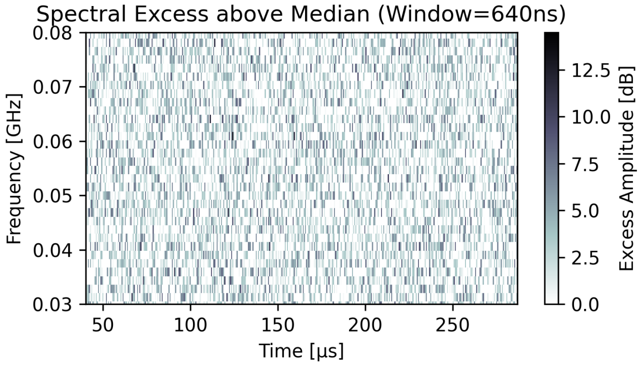

(a) 16 : 48 : 18 UTC.

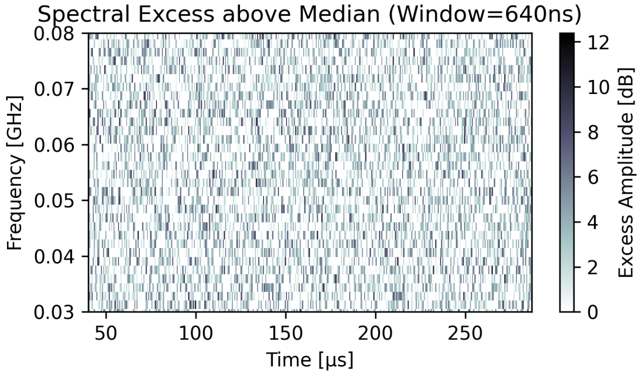

(b) 16 : 58 : 07 UTC.

Figure 26: Dynamic spectra plots of the LOFAR events on 09/10/2017.

A.4 Interferometric Sky Maps

The following figures are the interferometric sky maps from station CS002 of the LOFAR-event-matches that did not show a noticeable solar flare structure in the dynamic spectra.

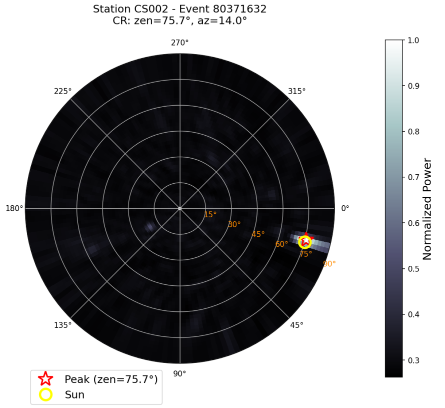

(a) 05 : 27 : 12 UTC.

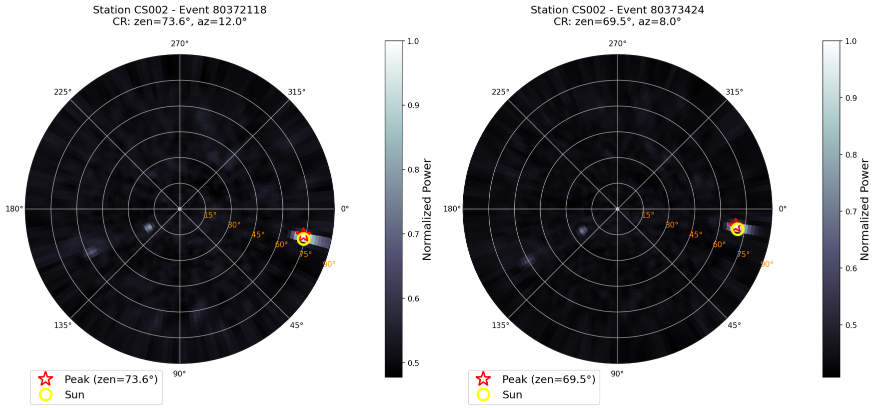

(b) 05 : 35 : 18 UTC.

(d) 05 : 57 : 04 UTC.

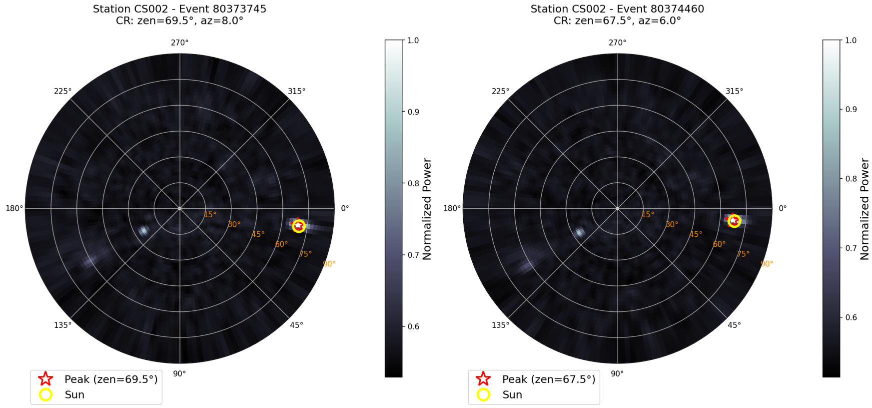

(c) 06 : 02 : 25 UTC.

(e) 06 : 14 : 20 UTC.

Figure 27: Interferometric sky maps of station CS002 of the LOFAR events on 07/19/2012. The signal seems to stem from the sun.

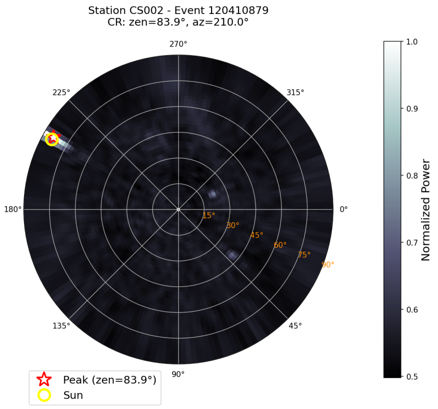

Figure 28: Interferometric sky map of station CS002 of the LOFAR event on 10/25/2013 at 15 : 27 : 59 UTC. The signal seems to stem from the Sun.

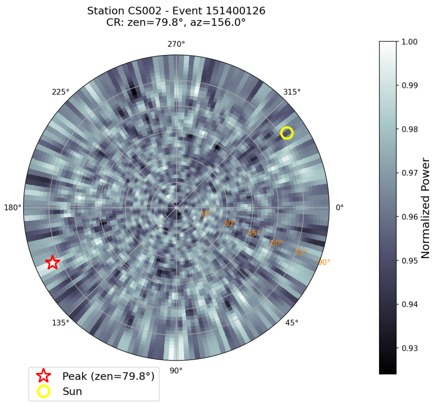

Figure 29: Interferometric sky map of station CS002 of the LOFAR event on 10/19/2014 at 07 : 35 : 26 UTC. The signal does not stem from the sun.

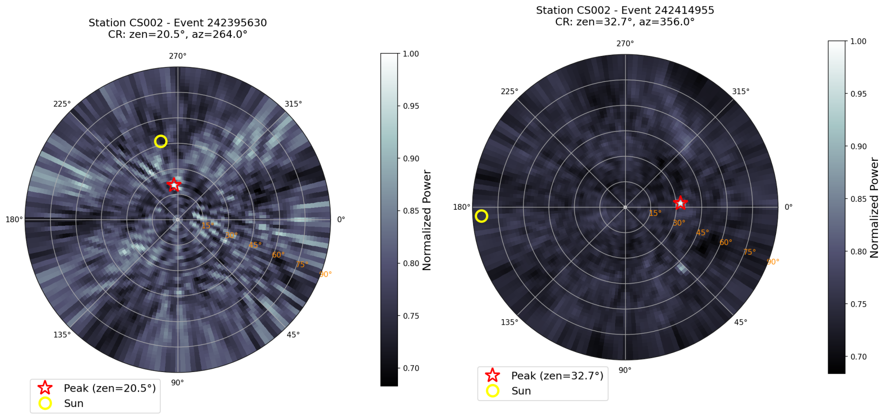

(a) 12 : 07 : 10 UTC.

(b) 17 : 29 : 15 UTC.

Figure 30: Interferometric sky maps of station CS002 of the LOFAR events on 09/06/2017. The signal does not stem from the sun.

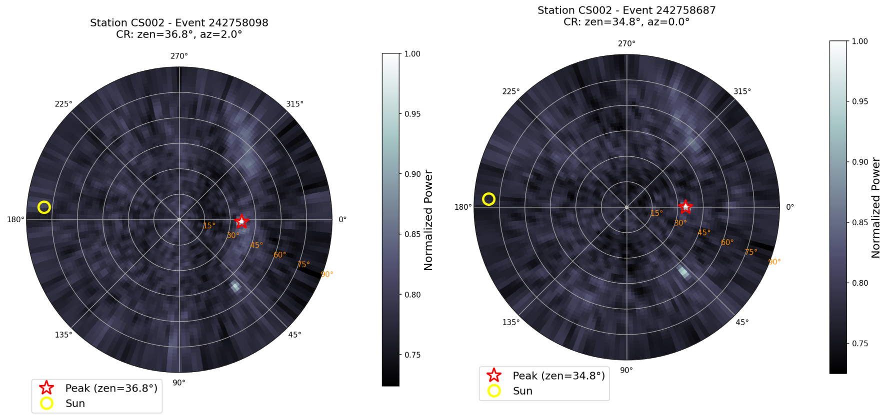

(a) 16 : 48 : 18 UTC.

(b) 16 : 58 : 07 UTC.

Figure 31: Interferometric sky maps of station CS002 of the LOFAR events on 09/10/2017. The signal does not stem from the sun.

A.5 Time-domain Plots

The following figures show the remaining time domain data plots of the LOFAR event on 09/10/2017 at 15 : 55 : 33.

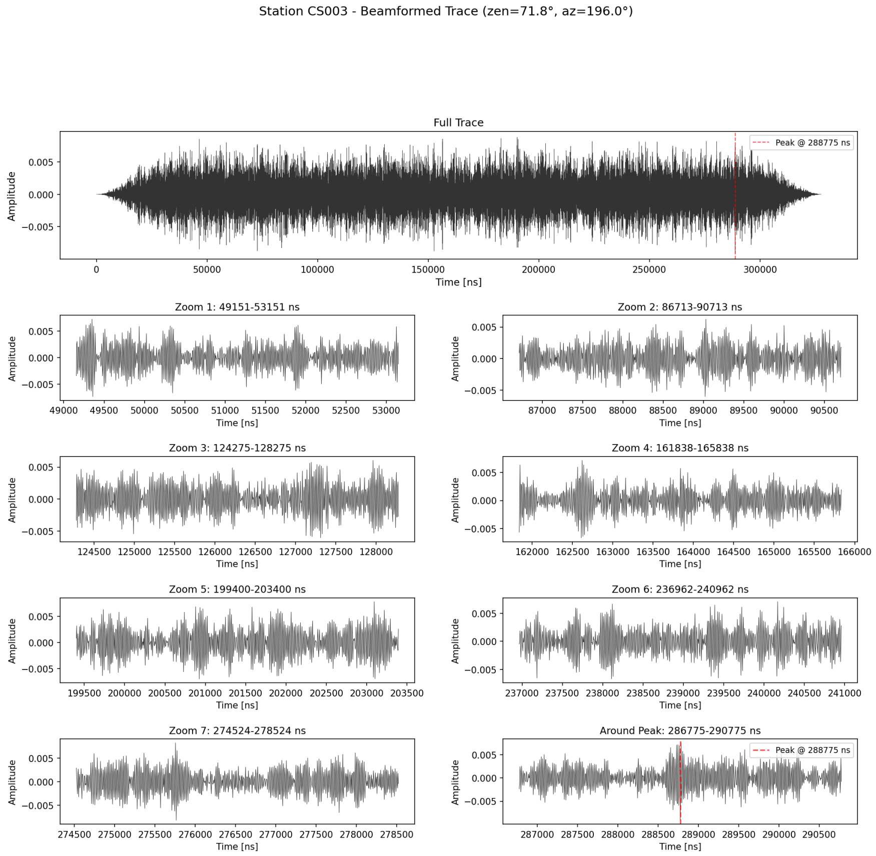

Figure 32: Time-domain plot for station CS003.

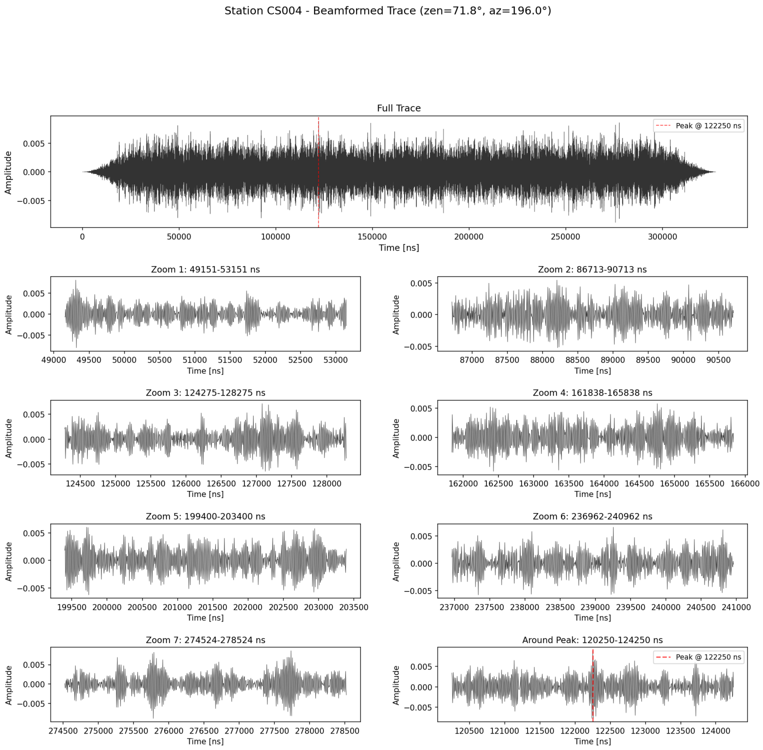

Figure 33: Time-domain plot for station CS004.

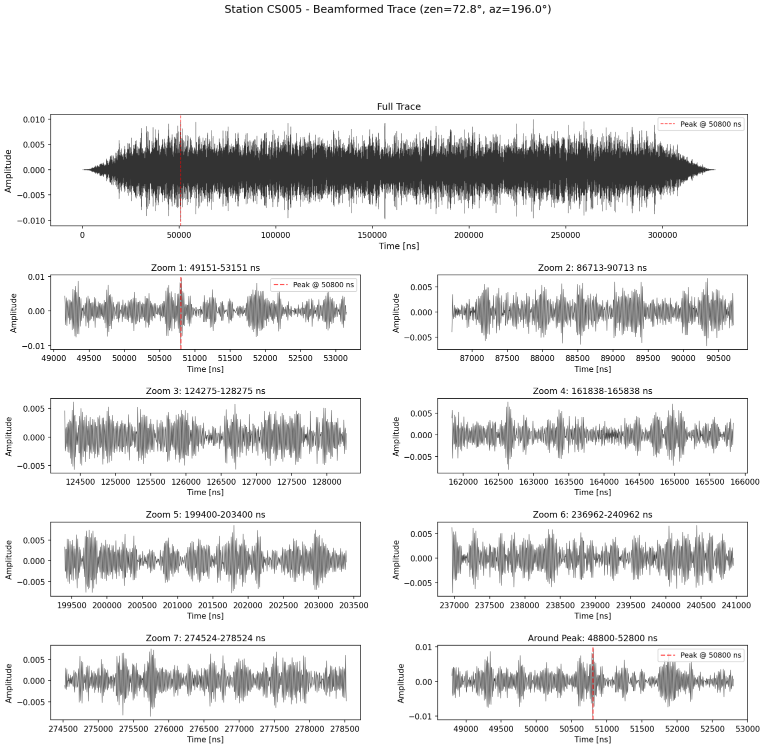

Figure 34: Time-domain plot for station CS005.

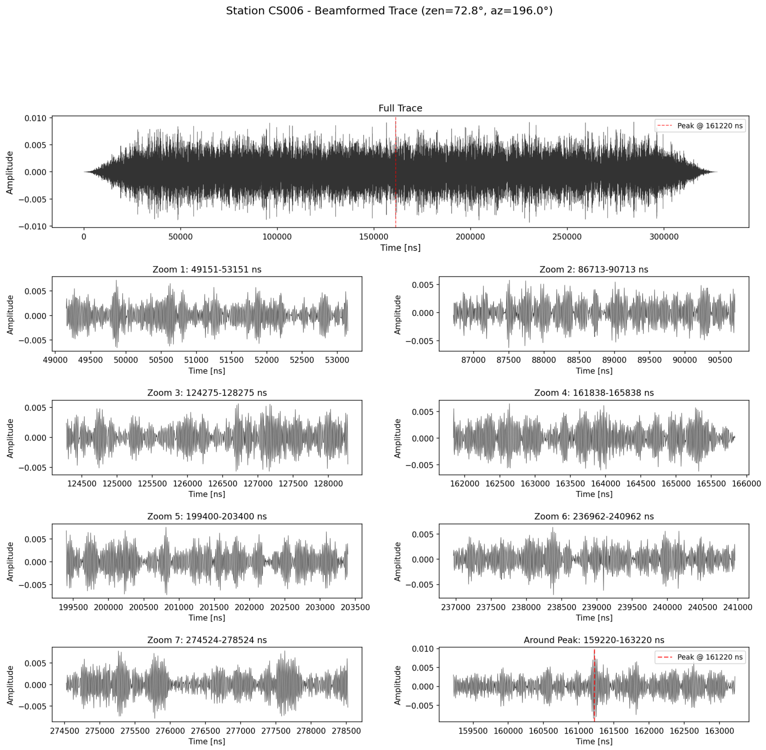

Figure 35: Time-domain plot for station CS006.

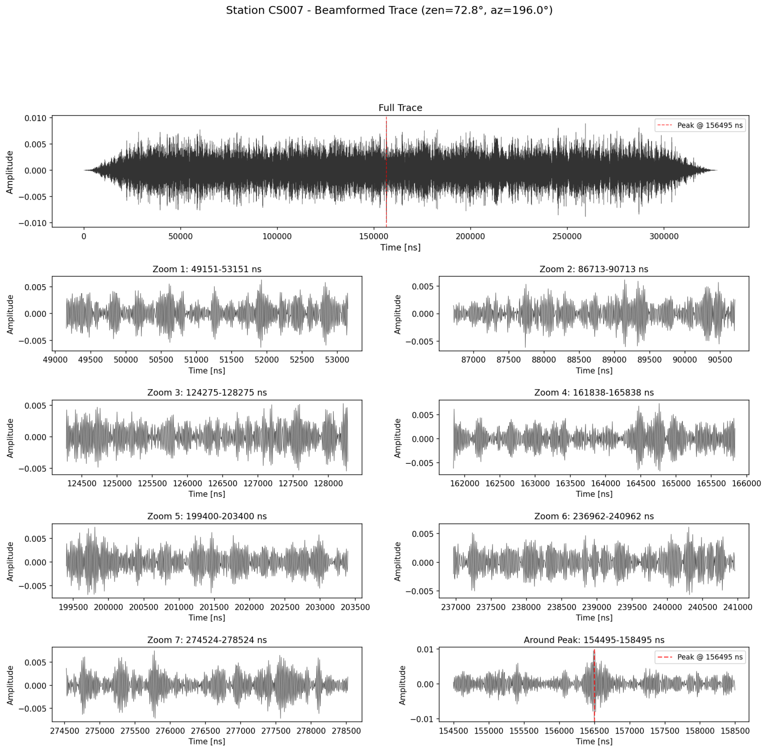

Figure 36: Time-domain plot for station CS007.

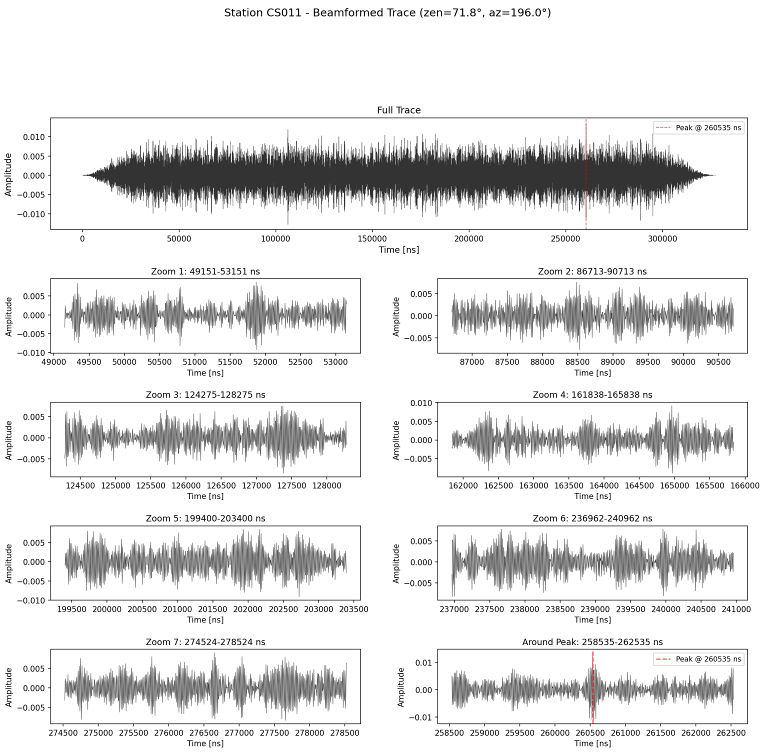

Figure 37: Time-domain plot for station CS011.

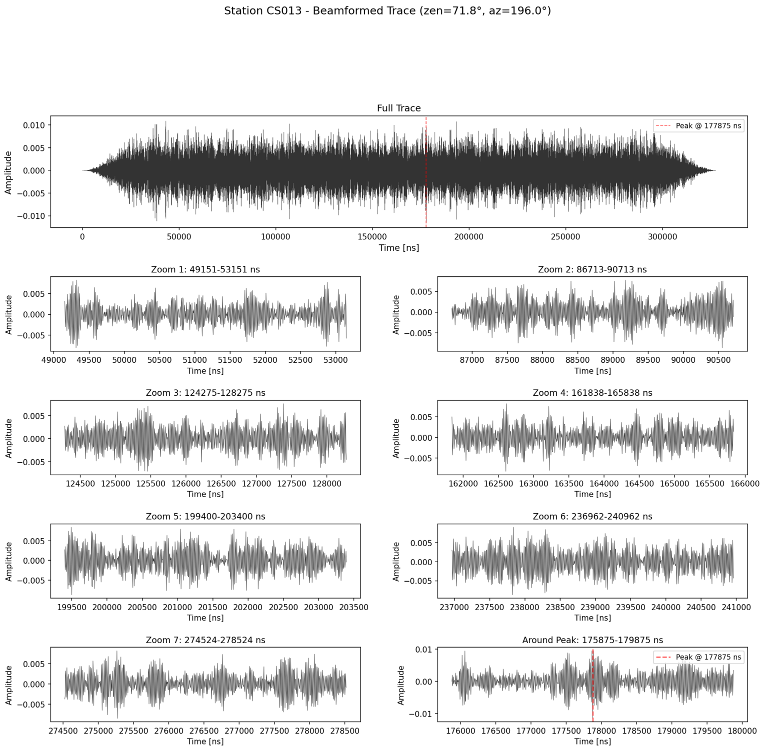

Figure 38: Time-domain plot for station CS013.

Bibliography.

[1] R. Hodgson. “On a curious Appearance seen in the Sun”. In: *Monthly Notices of the Royal Astronomical Society* 20.1 (Nov. 1859), pp. 15–16. ISSN: 0035-8711. DOI: `10.1093/mnras/20.1.15a`. eprint: `https://academic.oup.com/mnras/article-pdf/20/1/15/3059104/mnras20-0015a.pdf`. URL: `https://doi.org/10.1093/mnras/20.1.15a`.

[2] M. Piana, A. G. Emslie, A. M. Massone, B. R. Dennis. *Hard X-Ray Imaging of Solar Flares*. Springer Nature Switzerland AG, 2022.

[3] A. A. Krivolutsky, A. I. Repnev. “Impact of space energetic particles on the Earth’s atmosphere (a review)”. In: *Geomagnetism and Aeronomy* 52.6 (2012), pp. 685–716. ISSN: 1555-645X. DOI: `10.1134/S0016793212060060`. URL: `https://doi.org/10.1134/S0016793212060060`.

[4] M. P. van Haarlem, M. W. Wise, A. W. Gunst, G. Heald, et al. “LOFAR: The LOw-Frequency ARray”. In: *Astronomy amp; Astrophysics* 556 (July 2013), A2. ISSN: 1432-0746. DOI: `10.1051/0004-6361/201220873`. URL: `http://dx.doi.org/10.1051/0004-6361/201220873`.

[5] V. S. Airapetian, A. Glocer, G. V. Khazanov, R. O. P. Loyd, et al. “How Hospitable Are Space Weather Affected Habitable Zones? The Role of Ion Escape”. In: *The Astrophysical Journal Letters* 836.1 (2017), p. L3. DOI: `10.3847/2041-8213/836/1/L3`. URL: `https://doi.org/10.3847/2041-8213/836/1/L3`.

[6] K. Terveer, S. Bouma, S. Buitink, A. Corstanje, et al. “Cosmic ray detection with the LOFAR radio telescope”. In: *Proceedings of 10th International Workshop on Acoustic and Radio EeV Neutrino Detection Activities — PoS(ARENA2024)*. Vol. 470. 2024, p. 023. DOI: `10.22323/1.470.0023`.

[7] L. Fletcher, B. R. Dennis, H. S. Hudson, S. Krucker, et al. “An Observational Overview of Solar Flares”. In: *Space Science Reviews* 159.1–4 (Aug. 2011), 19–106. ISSN: 1572-9672. DOI: `10.1007/s11214-010-9701-8`. URL: `http://dx.doi.org/10.1007/s11214-010-9701-8`.

[8] C. More, A. Sharma. “Effect of Solar X-ray Flares on VLF Radio Wave Signal Strength at 19.8 and 24 kHz Received at Khatav (India) (16°46’N, 75° 53’E)”. In: (Jan. 2018).

[9] T. S. Bastian, A. O. Benz, D. E. Gary. “RADIO EMISSION FROM SOLAR FLARES”. In: *Annual Review Astronomy and Astrophysics. 36:131-188* (1998). URL: `https://doi.org/10.1146/annurev.astro.36.1.131`.

[10] S. M. White. “Solar Radio Bursts and Space Weather”. In: *Asian J. Phys.* 16 (Jan. 2007).

[11] S. Agarwal, J.A. Aguilar, S. Ali, P. Allison, et al. “Solar flare observations with the Radio Neutrino Observatory Greenland (RNO-G)”. In: *Astroparticle Physics* 164 (Jan. 2025), p. 103024. ISSN: 0927-6505. DOI: `10.1016/j.astropartphys.2024.103024`. URL: `http://dx.doi.org/10.1016/j.astropartphys.2024.103024`.

[12] D.B. Contreira, F.S. Rodrigues, K. Makita, C.G.M. Brum, et al. “An experiment to study solar flare effects on radio-communication signals”. In: *Advances in Space Research* 36.12 (2005). Space Weather, pp. 2455–2459. ISSN: 0273-1177. DOI: `https://doi.org/10.1016/j.asr.2004.03.019`. URL: `https://www.sciencedirect.com/science/article/pii/S027311770500013X`.

[13] V. Vasanth, Y. Chen, G. Michalek. “A wide-band high-frequency type-II solar radio burst”. In: *A&A* 702 (2025), A15. DOI: `10.1051/0004-6361/202554430`. URL: `https://doi.org/10.1051/0004-6361/202554430`.

[14] *Space weather prediction center - Solar Cycle Progression*. Accessed on 02/12/2026. URL: `https://www.swpc.noaa.gov/products/solar-cycle-progression`.

[15] *What is the solar cycle - National Environmental Satellite, Data, and Information Service*. Accessed on 02/12/2026. URL: `https://www.nesdis.noaa.gov/about/k-12-education/optical-phenomena/what-the-solar-cycle`.

[16] A. O. Benz, C. Monstein, H. Meyer, P. K. Manoharan, et al. “A World-Wide Net of Solar Radio Spectrometers: e-CALLISTO”. In: *Earth, Moon, and Planets* 104.1 (2009), pp. 277–285. ISSN: 1573-0794. DOI: `10.1007/s11038-008-9267-6`. URL: `https://doi.org/10.1007/s11038-008-9267-6`.

[17] *e-Callisto - International Network of Solar Radio Spectrometers, a Space Weather Instrument Array*. Accessed on 02/12/2026. URL: `https://www.e-callisto.org/index.html`.

[18] T. N. Woods, T. Eden, F. G. Eparvier, A. R. Jones, D. L. Woodraska, P. C. Chamberlin, J. L. Machol. “GOES-R Series X-Ray Sensor (XRS): 1. Design and Pre-Flight Calibration”. In: (11/21/2024). URL: `https://doi.org/10.1029/2024JA032925`.

[19] National Aeronautics and Space Administration. “GOES-R Series - Data Book”. In: (2019). Revision A. URL: `https://www.goes-r.gov/downloads/resources/documents/GOES-RSeriesDataBook.pdf`.

[20] J. Van Naarden, Dr. P. C. Griffith, Dr. D. Gall. “GOES-17 ADVANCED BASELINE IMAGER (ABI) POST LAUNCH TEST PERFORMANCE COMPARISON TO GOES-16”. In: *Proceedings for the 2018 EUMETSAT Meteorological Satellite Conference* (2018).

[21] P. T. M. Loto’aniu, A. Davis, A. Jarvis, M. Grotenhuis, et al. “Initial on-Orbit Results from the GOES-18 Spacecraft Science Magnetometer”. In: *Space Science Reviews* 219.8 (2023), p. 84. ISSN: 1572-9672. DOI: `10.1007/s11214-023-01032-3`. URL: `https://doi.org/10.1007/s11214-023-01032-3`.

[22] Lockheed Martin Space. “Geostationary Operational Environmental Satellite - R Series (GOES-U) - GOES-U Data Book”. In: (2024). Revision C. URL: `https://www.goes-r.gov/downloads/resources/documents/GOES-U%20DataBook.pdf`.

[23] J.A. Aguilar, P. Allison, J.J. Beatty, H. Bernhoff, et al. “Design and sensitivity of the Radio Neutrino Observatory in Greenland (RNO-G)”. In: *Journal of Instrumentation* 16.03 (2021), P03025. DOI: `10.1088/1748-0221/16/03/P03025`. URL: `https://doi.org/10.1088/1748-0221/16/03/P03025`.

[24] A. Vijai, B. Clark. "Status of First Neutrino Search". In: (2025). URL: `https://indico.cern.ch/event/1258933/contributions/6485827/attachments/3108214/5510759/rnog_icrc.pdf`.

[25] *Astron - LOFAR.* Accessed on 02/13/2026. URL: `https://www.astron.nl/telescopes/lofar/`.

[26] S. Thoudam, S. Buitink, A. Corstanje, J.E. Enriquez, et al. "LORA: A scintillator array for LOFAR to measure extensive air showers". In: *Nuclear Instruments and Methods in Physics Research Section A: Accelerators, Spectrometers, Detectors and Associated Equipment* 767 (2014), pp. 339–346. ISSN: 0168-9002. DOI: `https://doi.org/10.1016/j.nima.2014.08.021`. URL: `https://www.sciencedirect.com/science/article/pii/S0168900214009413`.

[27] K. Mulrey, S. Bouma, S. Buitink, A. Corstanje, et al. "Cosmic rays with LOFAR 2.0 - what's next?" In: *PoS* ARENA2024 (2024), p. 024. DOI: `10.22323/1.470.0024`.

[28] P. Schellart, A. Nelles, S. Buitink, A. Corstanje, et al. "Detecting cosmic rays with the LOFAR radio telescope". In: *A&A* 560 (2013), A98. DOI: `10.1051/0004-6361/201322683`. URL: `https://doi.org/10.1051/0004-6361/201322683`.

[29] C. Glaser, A. Nelles, I. Plaisier, C. Welling, et al. "NuRadioReco: a reconstruction framework for radio neutrino detectors". In: *The European Physical Journal C* 79.6 (2019), p. 464. ISSN: 1434-6052. DOI: `10.1140/epjc/s10052-019-6971-5`. URL: `https://doi.org/10.1140/epjc/s10052-019-6971-5`.

[30] *Space Weather Prediction Center - GOES X-Ray Flux.* Acessed on 03/04/2026. URL: `https://www.swpc.noaa.gov/products/goes-x-ray-flux`.

[31] D. E. Morosan, E. P. Carley, L. A. Hayes, S. A. Murray, et al. "Multiple regions of shock-accelerated particles during a solar coronal mass ejection". In: *Nature Astronomy* 3.5 (May 1, 2019), pp. 452–461. ISSN: 2397-3366. DOI: `10.1038/s41550-019-0689-z`. URL: `https://doi.org/10.1038/s41550-019-0689-z`.

[32] *Royal Observatory of Belgium - Callisto Burst Archives.* Accessed on 02/22/2026. URL: `https://sidc.be/humain/callisto_burst_archives`.

[33] *e-Callisto data - Search result for ALL STATIONS on 2017/09/10.* Accessed on 02/21/2026. URL: `https://astrodoncel.uah.es/dashboard/resultados.php?estacion=all&fecha=2017-09-10`.

[34] K. Terveer. *BeamformerSkyMapper.* 2026. URL: `https://github.com/nu-radio/NuRadioMC/blob/LOFAR_beamformer/NuRadioReco/modules/LOFAR/beamformerSkyMapper_LOFAR.py`.

[35] K. Terveer. *BeamformerSkyMapper Example.* 2026. URL: `https://github.com/nu-radio/NuRadioMC/blob/LOFAR_beamformer/NuRadioReco/examples/LOFAR/beamformer_sky_mapper_example.py`.

Acknowledgements

I want to thank everyone that supported me writing this thesis:

- To Prof. Dr. Anna Nelles, thank you for always having time for me and providing me with this exciting topic.
- To my supervisor at ECAP: Karen Terveer, for always taking the time to answer all of my questions and helping me with coding.
- To my parents and my sister: Thank you for your continuous support with everything I do.
- To my friends: Thank you for always being by my side.
- To my boyfriend Paul: Thank you for all the patience, the kindness and all the motivating words. Thank you for always supporting me.

Declaration of Originality

I, Lea Schneidhuber, student registration number: 23173770, hereby confirm that I completed the submitted work independently and without the unauthorized assistance of third parties and without the use of undisclosed and, in particular, unauthorized aids. This work has not been previously submitted in its current form or in a similar form to any other examination authorities and has not been accepted as part of an examination by any other examination authority.

Where the wording has been taken from other people's work or ideas, this has been properly acknowledged and referenced. This also applies to drawings, sketches, diagrams and sources from the Internet.

In particular, I am aware that the use of artificial intelligence is forbidden unless its use an aid has been expressly permitted by the examiner. This applies in particular to chatbots (especially ChatGPT) and such programs in general that can complete the tasks of the examination or parts thereof on my behalf.

Any infringements of the above rules constitute fraud or attempted fraud and shall lead to the examination being graded "fail" ("nicht bestanden").

Place, Date

Signature